

SmartEM: machine-learning guided electron microscopy

Yaron Meirovitch^{1,2,3,*}, Core Francisco Park^{1,2,*}, Lu Mi^{4,5,*}, Pavel Potocek^{6,7,*}, Shashata Sawmya⁴, Yicong Li⁸, Yuelong Wu^{1,3}, Richard Schalek^{1,3}, Hanspeter Pfister^{1,8}, Remco Schoenmakers⁶, Maurice Peemen⁶, Jeff W. Lichtman^{1,3,✉}, Aravinthan D.T. Samuel^{1,2,✉}, and Nir Shavit^{4,✉}

¹Center for Brain Science, Harvard University, Cambridge, MA 02138, USA

²Department of Physics, Harvard University, Cambridge, MA 02138, USA

³Department of Molecular and Cellular Biology, Harvard University, Cambridge, MA

⁴Computer Science and Artificial Intelligence Laboratory, Massachusetts Institute of Technology, MA

⁵Allen Institute for Brain Science, Seattle, WA

⁶Thermo Fisher Scientific, Eindhoven, the Netherlands

⁷Saarland University, 66123, Saarbrücken, Germany

⁸John A. Paulson School of Engineering and Applied Sciences, Harvard University, Boston, MA 02134, USA

*Equal contribution

Correspondence: aron.mr@gmail.com (YM); jeff@mcb.harvard.edu (JL); samuel@physics.harvard.edu (AS) shanir@csail.mit.edu (NS)

Summary

Connectomics provides essential nanometer-resolution, synapse-level maps of neural circuits to understand brain activity and behavior. However, few researchers have access to the high-throughput electron microscopes to rapidly generate the very large datasets needed for reconstructing whole circuits or brains. To date, machine-learning methods have been used after the collection of images by electron microscopy (EM) to accelerate and improve neuronal segmentation, synapse reconstruction and other data analysis. With the computational improvements in processing EM images, acquiring EM images has now become the rate-limiting step. Here, in order to speed up EM imaging, we integrate machine-learning into real-time image acquisition in a single-beam scanning electron microscope. This SmartEM approach allows an electron microscope to perform intelligent, data-aware imaging of specimens. SmartEM allocates the proper imaging time for each region of interest – scanning all pixels as rapidly, but then re-scanning small subareas more slowly where a higher quality signal is required in order to guarantee uniform segmentability of the entire field of view but with a significant time savings. We demonstrate that this pipeline achieves a 7-fold acceleration of image acquisition time for connectomics using a commercial single-beam SEM. We apply SmartEM to reconstruct a portion of mouse cortex with the same accuracy as traditional microscopy but in less time.

electron microscopy | connectomics | machine-learning | adaptive scanning

Introduction

Serial-section Electron Microscopy (ssEM) is widely used to reconstruct circuit wiring diagrams in entire brains of small animals like *C. elegans*, *Drosophila*, and zebrafish (White et al., 1986; Witvliet et al., 2021; Xu et al., 2020; Hildebrand et al., 2017) and brain regions in mammals (Morgan et al., 2016; Kasthuri et al., 2015; Bock et al., 2011; Abbott et al., 2020; Lu et al., 2023; Song et al., 2023). Comparing the growing numbers of connectomes of animals with different genetic backgrounds, life experiences, and diseases will illuminate the anatomical nature of learning, memory, and developmental plasticity, the nature of brain evolution, as well as the nature of anatomical abnormalities that cause neuropathology and disease (Kornfeld et al., 2020; Shapson-Coe et al., 2021; Loomba et al., 2022; Karlupia et al., 2023; Bidel et al., 2023). To achieve wide-scale deployment for comparative connectomics, data acquisition and analysis pipelines need to

become more widely available (Swanson and Lichtman, 2016). At present, connectome datasets are mostly acquired by the few laboratories and institutions equipped with specialized and expensive high-throughput electron microscopes such as the TEMCA (Transmission Electron Microscopy Camera Array) or the Zeiss 61- or 91-beam scanning electron microscope (SEM) (Bock et al., 2011; Shapson-Coe et al., 2021). Until recently, dataset acquisition had not been a limiting factor in connectomics (Lichtman et al., 2014). A more significant bottleneck had been data analysis – segmenting serial-section electron micrographs to reconstruct the shape and distribution of nerve fibers, identify synapses, and map circuit connectivity. However, recent improvements in machine-learning and image analysis (Beier et al., 2017; Januszewski et al., 2018; Meirovitch et al., 2019; Sheridan et al., 2023) have dramatically sped data analysis, creating a now urgent need for faster image acquisition. The field needs more electron microscopes to deliver datasets as fast as they can now be analyzed. One way to meet this need is to enable widely-available electron microscopes, like more affordable point-scanning SEMs, to collect connectomic datasets.

When using a point-scanning SEM for connectomics, the time budget for image acquisition is mostly the dwell time that the electron beam spends on each pixel. In practice, SEM imaging of well-prepared, high-contrast, electron-dense tissue for connectomics usually uses dwell times $\geq \sim 1000$ ns/pixel. By comparison, the time spent moving the beam between pixels is negligible; modern SEMs use electrostatic scan generators that deflect the electron beam to any pixel in an image (Mohammed and Abdullah, 2018; Anderson et al., 2013). To accelerate an SEM for connectomics, one must reduce the total dwell time over all pixels, but without losing information needed to accurately determine the wiring diagram.

For connectomics, the salient measure of image accuracy is neuronal segmentation – being able to correctly identify each neuron’s membrane boundary and to correctly identify each synapse. In standard SEM, image acquisition is done by specifying a fixed homogeneous dwell time for all pixels. The longer the dwell time, the higher the signal-to-noise per pixel, and the more accurate the segmentation. Thus, there is a fundamental trade-off between SEM imaging time and segmentation accuracy. Previous approaches to improving segmentation accuracy with rapidly acquired images have involved post-acquisition image processing such as de-noising (Minnen

et al., 2021) or “super-resolution”/upsampling (Fang et al., 2021). However, image processing that works entirely after the completion of image acquisition is limited by the amount of original information acquired. No technique unambiguously “creates” information that was not acquired in the first place. Fast, lossy image acquisition can miss critical information that precludes accuracy in any subsequent segmentation.

Our solution to the problem of missing information in an initial rapidly acquired image is to immediately recover information during real-time microscope performance. To do this, we developed a “smart” SEM pipeline that rapidly identifies error-prone regions as well as high-salience regions (such as synapses) in every rapidly acquired image, and immediately and slowly re-scans only these regions. We define error-prone regions as only those that would confer full segmentation accuracy to a composite image, which is built from the initial rapidly acquired image (adequate wherever segmentation is accurate at short dwell time) and fused with long dwell time re-scans (necessary wherever segmentation is error-prone). When error-prone and high-salience regions are relatively few in number and small in size, re-scanning adds little to the total image acquisition time budget while fully restoring segmentation accuracy. We sought an image acquisition pipeline that achieves the accuracy of uniform long dwell time acquisition with nearly the speed of uniform short dwell time acquisition.

We implemented smartness in the pipeline with machine-learning algorithms running within SEM computer hardware. This pipeline, called SmartEM, can be applied in any context where images exhibit high spatial heterogeneity in segmentation accuracy as a function of imaging time – a fundamental characteristic of brain images where nerve fibers and synapses can vary in size and density from region to region. Unavoidable spatial heterogeneity in any specimen is why a smart selection of which regions to collect at short dwell times and which regions to re-scan at long dwell times can achieve full segmentation accuracy but with much less total dwell time. Applied to connectomics, the SmartEM pipeline yields a substantial 7-fold speedup for a widely available point-scanning SEM, allowing the microscope to be used for connectomics solely by implementing our machine-learning algorithms in the GPU-equipped SEM support computer. Spatial heterogeneity characterizes numerous SEM applications, and SmartEM can thus be applied to speed reconstruction of other specimens in biology, in material sciences and in electronic circuit fabrication.

Results

Suitability of adaptive dwell times for connectomics

To establish the rationale for our connectomics pipeline by point-scanning SEM – automatically applying short dwell times to most brain regions that are “easy” to segment and long dwell times to fewer brain regions that are “hard” to segment – we quantitatively tested how spatial heterogeneity in representative mammalian brain images affects segmentation accuracy with different dwell times. To perform these tests, we used a recent high-quality sample comprising 94 sections of mouse visual cortex (Karlupia et al., 2023). We re-imaged these 94 sections at 4 nm pixel resolution using a point-scanning Verios G4 UC

SEM from Thermo Fisher Scientific and a range of fixed dwell times from 25 to 1200 ns/pixel.

We note that when these images were originally acquired in a previous study using standard point-scanning SEM, the dwell time was 800 ns/pixel (Karlupia et al., 2023). This dwell time was determined by a “rule-of-thumb” and is close to the 800 – 1000 ns/pixel needed for maximal segmentation accuracy for this dataset (Figure 1A, 1B).

Our segmentation algorithm – mapping EM images to membrane predictions (EM2MB) followed by a standard watershed transform – provided an objective assessment of segmentation accuracy of images collected with different dwell times. We adapted EM2MB to SEM images taken with different dwell-times (see Supplement). We automatically segmented 256 randomly selected 2000×2000 pixel regions taken from the 94-section sample with different dwell times. Automatic segmentation with ultrafast dwell times (25 ns/pixel) produced frequent merge and split errors compared to automatic segmentation of the same regions with overly slow dwell times (1200 ns/pixel) (Figure 1A). As dwell times increased, segmentation errors gradually disappeared.

To quantify segmentation accuracy, we calculated the Variation of Information (VI; Meila (2003)) between each automatically segmented region at each faster dwell time and the segmentation obtained at the slowest dwell time (Figure 1B). Segmentation accuracy increased with slower dwell times, and saturated at 800-1000 ns/pixel, consistent with the rule-of-thumb practice in choosing the dwell times for connectomics. With >1000 ns dwell times, segmentation accuracy using EM2MB is saturated. At 25 ns/pixel, acquisition speed is 40× faster than at 1000 ns/pixel, but with lower accuracy.

Brain tissue is typically heterogeneous in the difficulty of segmentation across image regions (Figure 1C, 1D). Thus, segmentation accuracy varied substantially from region to region. For slow dwell times (1000 ns), segmentation accuracy was narrowly distributed around small VI, indicating less segmentation errors. For ultrafast dwell times (25 ns), segmentation accuracy was broadly distributed. Some regions exhibited the same low VI with both ultrafast and slow dwell times (“easy” to segment regions). Some regions exhibited drastically higher VI for ultrafast dwell times than slow dwell times (“hard” to segment regions) (Figure 1C). For each region, we determined the minimum dwell time to reach the same segmentation accuracy as the slowest dwell time (see Supplement: Determination of maximal segmentation quality). We observed a broad distribution of minimum dwell times across pixel regions. Most 2000×2000 pixel regions are accurately segmented with dwell times <150 ns, but a small number (~25%) required longer dwell times. Minimum dwell times exhibited a broad-tailed distribution from 50 – 1200 ns/pixel (Figure 1D).

Challenges in smart microscopy

We sought a SmartEM pipeline to identify and adapt to spatial heterogeneity in the segmentation accuracy of brain tissue for connectomics when imaged at different dwell times. To implement this pipeline with a point-scanning SEM, we needed to solve several challenges. The SEM needs to automatically

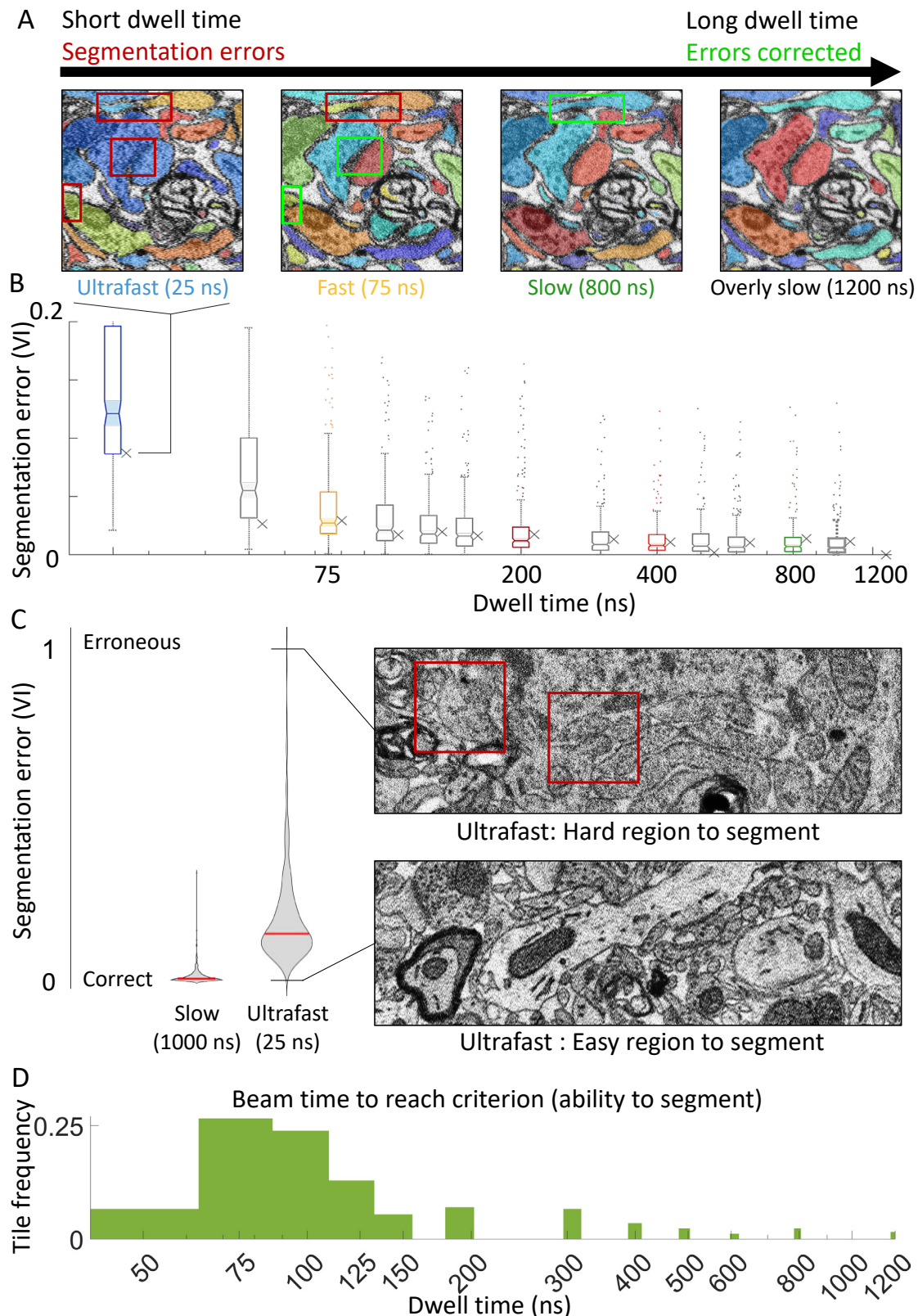


Figure 1. The effect of the beam's dwell time on the ability to segment the EM into neuronal elements. **A.** Scanning the same EM tile with different dwell times. Short dwell time scans result in segmentation errors (red squares) that are resolved by longer scans (green squares). Increasing the dwell time improves the segmentation accuracy of short dwell time images (25 ns/pixel and 75 ns/pixel) but does not improve the segmentation accuracy of sufficiently long dwell time images (800 ns/pixel). **B.** The segmentation quality of the same images used in (A) are represented by x markers, alongside the distribution of segmentation qualities of 256 images (scatter and boxes) for 13 dwell times, from 25 ns to 1000 ns, calculated relative to a reference image taken at 1200 ns/pixel. Segmentation error is quantified by variation of information (y-axis). VI drops rapidly with increased dwell times, saturating with dwell times near 800 ns. Wide distributions indicated by whiskers at each dwell time indicate that some image tiles can be segmented at any dwell time. **C.** Segmentation of neuronal tissue has varying quality due to tissue heterogeneity: taking an image at 25 ns could lead to an image that can be segmented at high quality (bottom image) or low quality (top image), compared to taking the images slowly (at 1000 ns). **D.** The majority of image regions (green areas add up to 1.00) can be segmented at faster dwell times (75 ns to 125 ns), while some regions require longer dwell times (between 400 ns to 800 ns) to reach the segmentation quality criterion. Thus, adapting dwell time for different regions would save imaging time without reducing segmentation quality.

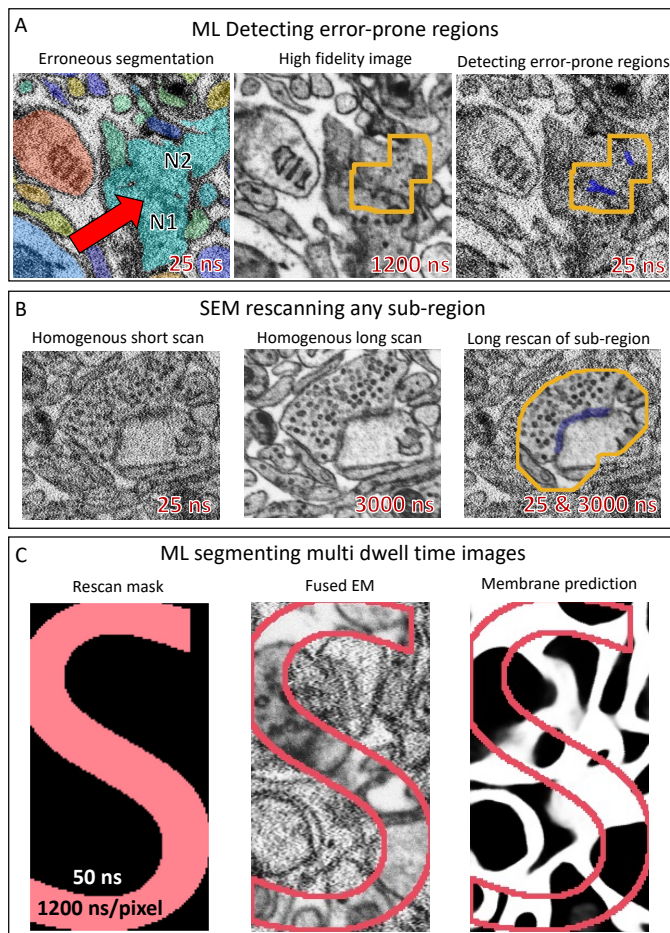


Figure 2. Smart microscope challenges. **A.** An erroneous segmentation of a rapidly acquired image (25 ns/pixel) with a red arrow indicating the location of a merge error between two neurons (N1, N2). Slowly acquiring the same image at 1200 ns/pixel captures the neuronal boundary (middle). The output of the ERRNET neural network that was trained to predict segmentation errors from EM is shown on the right. Blue indicates the location where the network predicts a possible merge or a split error. The yellow outline is a window around the predicted error to provide further context needed for downstream correction. **B.** The SEM readily captures any part of an image at different dwell times, homogeneously at short dwell times (left), homogeneously at long dwell times (middle), or homogeneously at short dwell times with a sub-region taken at long dwell times (right). Here, the yellow outline for the long dwell time sub-region contains a synaptic cleft. **C.** Predicting neuronal borders from fused EM images using FUSED2MB.

174 identify error-prone locations in an initial rapidly acquired brain
 175 image. The SEM needs to immediately re-scan pixel neigh-
 176 borhoods around error-causing locations to guarantee accurate
 177 segmentation. After image acquisition, the pipeline needs to ac-
 178 curately segment composite images built from the initial rapidly
 179 acquired images fused with re-scanned error-prone regions. We
 180 review solutions to these challenges that we incorporate in the
 181 smart microscopy pipeline described below.

182 **Detecting error-prone regions by an SEM.** To identify error-
 183 prone regions in initial rapidly acquired images, we developed
 184 a machine learning (ML) algorithm to run on the microscope's
 185 support computer. **Figure 2A** shows a rapidly acquired image
 186 tile and its segmentation containing a merge error (red arrow
 187 in left panel); the slowly acquired image tile that would not
 188 produce an error (middle panel); the prediction of a neural
 189 network (ERRNET, see below) that identifies error-causing

190 locations in the rapidly acquired image (corresponding to cell
 191 membranes associated with the merge error, highlighted in
 192 blue in right panel); and the specification of error-prone region
 193 to be re-scanned that would remedy segmentation errors in
 194 post-processing (yellow outline in middle and right panels).
 195 ERRNET operates in real-time within SEM computer hardware
 196 that is equipped with a high-performance GPU, and is much
 197 faster than initial image acquisition – per pixel processing for a
 198 single commodity GPU is <100 ns/pixel; N GPUs operating in
 199 parallel require < 100/ N ns/pixel. A related idea where EM
 200 acquisition is guided based on uncertainty measures estimated
 201 by neural network models was described in [Shavit et al. \(2021\)](#).

202 **SEM re-scanning any sub-region.** To use the prediction of error-
 203 prone regions during real-time SEM operation, we modified the
 204 scanning procedure of the microscope to re-scan error-prone
 205 regions at slow dwell times right after the fast scan. In addition
 206 to re-scanning error-prone regions, neural networks can be
 207 trained for data-aware re-scan of additional regions of interest
 208 like synaptic clefts for applications in connectomics. **Figure 2B**
 209 depicts data-aware re-scan where the microscope is guided to
 210 re-take regions around synaptic clefts that are predicted from an
 211 initial fast scan image of a section of mammalian cortex. SEM
 212 microscopes with electrostatic scan generators are able to con-
 213 duct efficient and rapid re-scan without wasted time in moving
 214 the electron beam ([Mohammed and Abdullah, 2018](#); [Anderson
 215 et al., 2013](#)). When ERRNET and re-scan software are seam-
 216 lessly integrated within SEM computer hardware (see below),
 217 the total time spent acquiring an image is the total number of
 218 pixels \times the short initial dwell time plus the total number of
 219 re-scanned pixels \times their long dwell time.

220 **Segmentation of multi-dwell time images.** After image ac-
 221 quisition, a smart microscopy pipeline generates a complete
 222 rapidly acquired image and set of slowly re-scanned regions
 223 of each sample. When pixels from the re-scanned regions are
 224 substituted into corresponding locations in initially rapidly
 225 acquired images, composite images are produced with pixels
 226 of multiple dwell times. Previous segmentation algorithms
 227 for connectomics have dealt with a single pre-fixed dwell
 228 time ([Januszewski et al., 2018](#); [Meirovitch et al., 2019](#);
 229 [Sheridan et al., 2023](#)) – these algorithms generalize poorly
 230 to homogeneous images taken at different dwell times or to
 231 heterogeneous images composed of regions taken at different
 232 dwell times. The smart microscopy pipeline demands new
 233 algorithms to accurately segment composite images where
 234 different regions are obtained at different dwell times. We
 235 developed a data augmentation training procedure technique
 236 for a neural network with a U-Net ([Ronneberger et al., 2015](#))
 237 architecture (FUSED2MB) to accurately detect membranes
 238 in an image with heterogeneous dwell times as well as if the
 239 image was taken with a single uniformly applied dwell time
 240 (see **Supplement**). **Figure 2C** shows an example of an image
 241 that has multiple dwell times (slow scanning arbitrarily within
 242 an S-shaped region surrounded by fast scanning). The predicted
 243 membranes by FUSED2MB are unperturbed when crossing
 244 between regions taken with different dwell times.

245 Thus, the challenges in building a smart microscopy

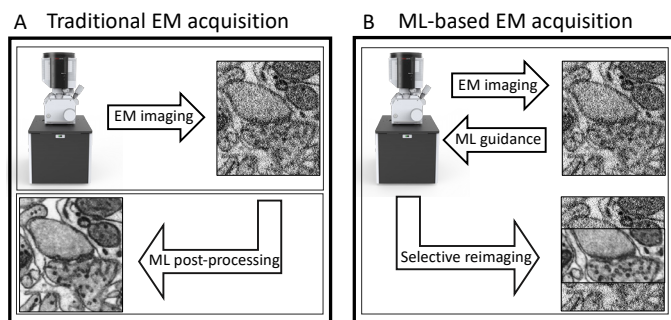


Figure 3. Traditional versus ML-based image acquisition. **A.** Traditional microscopes acquire images without real-time adaptation to the data itself. Acquired images are often processed off-line using machine learning algorithms that might enhance the existing information content (e.g. using super resolution, de-noising and in-painting ML techniques). **B.** The SmartEM pipeline uses dataset-specific machine learning algorithms to guide image acquisition in real-time to increase information content.

pipeline are met by extensively using machine learning in both guiding image acquisition and image analysis. As illustrated in **Figure 3**, our pipeline differs from previous applications of machine learning in electron microscopy, where image analysis using neural networks was only used to improve image appearance after image acquisition.

The smart microscopy pipeline

We built an integrated smart pipeline that meets the above challenges, **Figure 4A** shows an example of our smart microscopy pipeline run on a small tile from the mouse cortex dataset (Karlupia et al., 2023). The components of the SmartEM are outlined in **Figure 4B** and their design and implementation are described below in detail.

Determining the standard dwell time needed for high accuracy segmentation. The goal of the SmartEM pipeline is to reach the segmentation accuracy of standard SEM with uniform slow scanning, but in much less time. To fairly assess the improvement of SmartEM over standard SEM, we needed first to determine the shortest dwell time for standard imaging that leads to accurate segmentation (800 – 1000 ns/pixel in the example in **Figure 1B**).

We also needed an objective metric for assessing accurate segmentation. In the example shown in **Figure 1B**, the microscope automatically estimates 800 ns as the minimal dwell time needed for accurate segmentation. This estimate was based on the output of automatic membrane prediction by a neural network (Pavarino et al., 2023).

To accomplish this, we trained a neural network called SLOWEM2MB to perform automatic membrane prediction using long dwell time images. We acquired a small and diverse subset of long dwell time images from random locations in a specimen, typically twenty $5 \times 5 \mu\text{m}$ EM tiles, and performed manual segmentation by an expert to create training data for SLOWEM2MB.

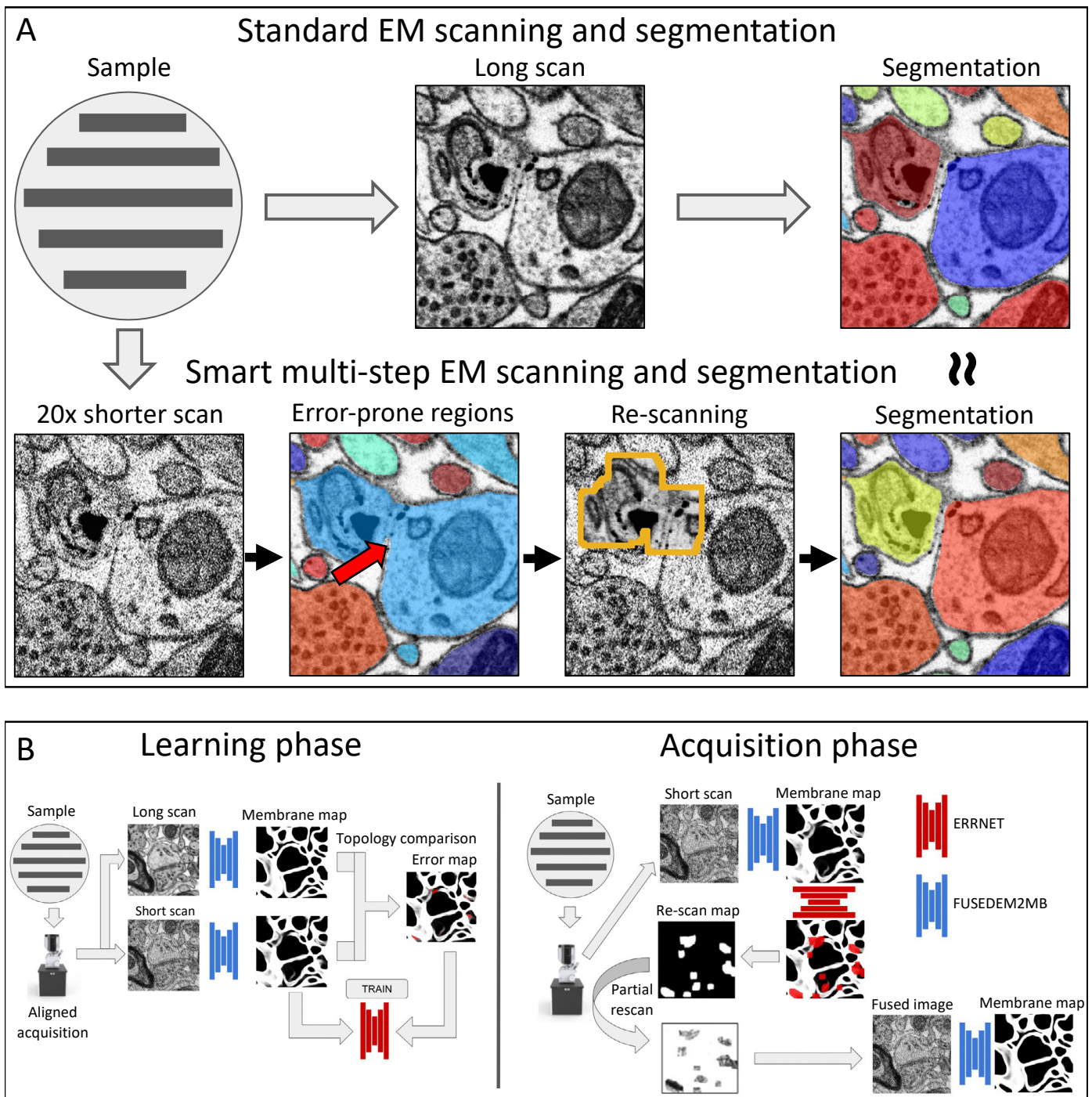
Next, we used SLOWEM2MB to train a separate neural network called EM2MB that was capable of predicting membranes with long or short dwell time images. The single-beam SEM allowed repeatedly re-imaging the same region at different dwell times. In this way it was possible to guide the microscope to collect a large sample of EM images from different random

locations in the specimen, using different dwell times ranging from 25 to 2500 ns/pixel as shown in **Figure 4**. SLOWEM2MB was applied to the long dwell time image at each location to automatically create segmentations that we could use as “ground truth” to train EM2MB to predict segmentations with long or short dwell time images. Both SLOWEM2MB and EM2MB were implemented using a U-net architecture.

SLOWEM2MB and EM2MB calculated the trade-off between pixel dwell time and segmentation accuracy. EM2MB was used to automatically segment all dwell time images (e.g. from 25 to 1000 ns/pixel for the mouse cortex dataset) and compare them to a reference automatic segmentation corresponding to the longest dwell time image (e.g. 1200 ns/pixel image). Thus, it was possible to identify the shortest dwell time for which mean accuracy across tiles was not further improved by longer dwell time imaging. This minimum dwell time was defined by SmartEM as the required dwell time to achieve maximum segmentation accuracy at a defined spatial resolution.

Learning to detect error-causing locations in short dwell time images. To further reduce imaging time we adjusted pixel dwell time based on segmentation accuracy. Most image regions can be segmented with full accuracy after scanning with a short dwell time. Additional dwell time is only selected for those regions that require longer imaging to segment properly. This selection was accomplished via a neural network (ERRNET) that learned what regions required longer dwell time after scanning whole images with short dwell time. ERRNET learns the features of error-causing locations in raw short dwell time images that produce segmentation differences – erroneous merges or splits – in comparison to long dwell time images.

To assemble “ground-truth” to train ERRNET, the microscope first takes a large set of images from random locations in the specimen at multiple dwell times (e.g. from 25 to 1200 ns/pixel). These images are segmented to distinctly label every contiguous neuron cross section. Automatic labeling can be done using membrane probabilities, a seeding procedure, and a standard region-growing algorithm such as watershed (Vincent and Soille, 1991). Segmented images at all dwell times are compared to reference segmented images taken with the longest dwell time (1200 ns/pixel for the mouse cortex dataset in **Figures 1A, 1B**, longer than needed for fully accurate segmentation with SLOWEM2MB). To automatically learn segmentation discrepancies between short and long dwell time images, we developed a method to produce a binary error mask that defines the morphological differences between two segmented images based on the variation of information (VI) clustering metric (Meila, 2003) (See **Supplement** for details). We trained ERRNET to predict error-causing regions in short dwell time image as shown in **Figure 4**. We used the VI metric to detect objects that are morphologically different between segmentations of short and long dwell time images, and then mapped the borders that differ for these objects (described in **Supplement**) (Meila, 2003). We noted that all segmentation errors in short dwell time images can be repaired (i.e. leading to identical segmentation as long dwell time images) by selectively replacing only regions surrounding discrepancy-causing locations in short dwell time images with corresponding regions taken from long



343 dwell time images.

344 **Detecting error-prone regions in short dwell time images,**
345 **re-scanning, and producing fused images.** In real-time opera-
346 tion, the SEM microscope must take an initial rapidly acquired
347 image, execute ERRNET to detect error-prone locations, define
348 a re-scan mask by padding error-prone locations to capture
349 enough context to improve segmentation accuracy, and then
350 immediately re-scan all error-prone regions using slow dwell
351 times.

352 **Unifying and enhancing images.** The final output of the pipeline
353 are images where some pixels are captured with slower dwell
354 times than others. Although the raw appearance of rapidly cap-
355 tured regions (high pixel noise) and slowly captured regions
356 (low pixel noise) does not degrade segmentation accuracy, it
357 does create visually unappealing contrasts (**Figure 3B**). To stan-
358 dardize the SmartEM image for human interpretation, we also
359 built an algorithm that translates the style of the SmartEM im-
360 ages to look like standard EM images with homogeneous dwell
361 times. A similar technique was described in [Shavit et al. \(2021,](#)
362 [2023\)](#). This stylized output does not supplant, but is saved in
363 addition to, the raw composite SmartEM images. We note that
364 stylized images often retain the correct details of the ultrastruc-
365 ture seen in homogeneous long dwell time images (**Figure S8**).

366 **Technique Evaluation**

367 We developed our SmartEM pipeline to expedite connectomic
368 reconstruction on our widely available point-scanning SEM, the
369 Verios G4 UC from Thermo Fisher Scientific. Here, we quanti-
370 tatively estimate the practical improvement in quality and speed
371 offered by this pipeline for connectomics.

372 **Improving accuracy.** One premise of the smart microscopy
373 pipeline is that automatically detecting error-prone regions
374 and replacing them with slower dwell time pixels will reduce
375 segmentation errors. To attempt to validate this premise, we
376 compared the accuracy of a segmentation pipeline trained
377 to deal with short dwell time images (FASTEM2MB at 100
378 ns/pixel) to a SmartEM pipeline trained to deal with composite
379 images made from short and long dwell times (FUSED2MB
380 at 100 ns/pixel and 2500 ns/pixel). The performance of these
381 networks was compared to the standard segmentation pipeline
382 with slow image acquisition (SLOWEM2MB at 2500 ns/pixel).
383 For fair comparison, we used the same long dwell time for the
384 re-scanning in the smartEM pipeline and for the uniform scan
385 in the standard pipeline. We found that using these dwell times,
386 SmartEM pipeline is $\sim 5\times$ faster than the standard segmentation
387 pipeline with slow image acquisition and $\sim 2-3\times$ more accurate
388 (based on VI) than the standard pipeline operating quickly (100
389 ns/pixel) (**Figure S2**). Thus, fusing long dwell time pixels into
390 a rapidly acquired image can improve segmentation accuracy.

391 Another premise of the SmartEM pipeline is that given the
392 additional time spent in re-scanning part of an image, the im-
393 provement in segmentation accuracy is superior to the improve-
394 ment that would be obtained by giving the same amount of extra
395 time to a standard pipeline that somewhat more slowly acquires
396 all pixels at the same dwell time. To attempt to validate this

premise, we used a FastEM pipeline by choosing competitively
fast settings for the standard pipeline, with pixels taken homoge-
neously at 75 ns. We compared the performance of FastEM with
a SmartEM pipeline tuned to take the same average time when
combining both the initial scan and the smart re-scan. The initial
SmartEM scan dwell time was set to 25 ns, the re-scan dwell
time to 200 ns, and a portion of the 12.5% most "error suscepti-
ble" regions were adaptively selected per tile for re-scan, so as
to provide an exact average of 75 ns/pixel. We compared the
variation of information of $N=64$ segmented 2048×2048 pixel
image tiles of fastEM and SmartEM to a reference slowEM and
found that the SmartEM had less error (non-parametric paired
sample test; $p<0.05$ and $p<0.025$ for 38 tile devoid of cell bod-
ies).

Estimating speed-up. We considered two scenarios for the
large-scale collection of a connectome dataset. The first
involves a fixed imaging time budget to acquire a selected data
volume at the selected pixel resolution. Here, the task is to
intelligently allocate the imaging time to optimize segmentation
accuracy. We note that this optimization is not feasible with a
standard EM pipeline that would fix the homogeneous dwell
time to fill the time budget. The second scenario involves set-
ting the pipeline quality according to the quality of a standard
EM imaging pipeline. Here, the task is to determine SmartEM
parameters that maintain this quality while minimizing the
required imaging time per volume. Below we analyze both
scenarios.

Scenario 1: Optimized accuracy with fixed imaging time budget
We fix the total imaging time budget for a given spec-
imen. From this requirement the pixel dwell time is determined
after subtracting overhead factors (such as image focusing,
astigmatism correction, and mechanical stage movement) from
the total budget. For example, the user might need to image a
given specimen – $100\times 100\times 100\ \mu\text{m}$ tissue, cut in 30 nm thick
sections, imaged at 4 nm spatial resolution – within 5 days
of continuous EM operation. These constraints determine the
average dwell time per pixel

$$\frac{(5 \cdot 24 \cdot 3600 \text{ sec})(4^2 \cdot 30 \text{ nm}^3)}{(100\ \mu\text{m})^3} = 207.36 \text{ ns.}$$

For a standard EM pipeline, 207.36 ns becomes the homo-
geneous pixel dwell time. For the SmartEM pipeline, the initial
scan and re-scan of all error-prone regions should sum to an av-
erage of 207.36 ns/pixel. This average dwell time, which we
call *effective dwell time*, can be achieved with different combi-
nations of initial fast dwell time, re-scan slow dwell time, and
percentage of re-scanned pixels:

$$T_{\text{effective}} = T_{\text{initial}} + \alpha \cdot T_{\text{re-scan}}$$

where T represents dwell times.

For example, an effective average dwell time of 207.6 ns is
achieved with an initial dwell time of $T_{\text{initial}} = 100$ ns, re-scan
rate of $\alpha = 5\%$, and re-scan dwell time of $T_{\text{re-scan}} = (207.36 -$
 $100)/0.05 = 2147.2$ ns. These parameter settings correspond to
a specific segmentation accuracy (VI) relative to the reference
homogeneous long scan image. SmartEM considers a grid of

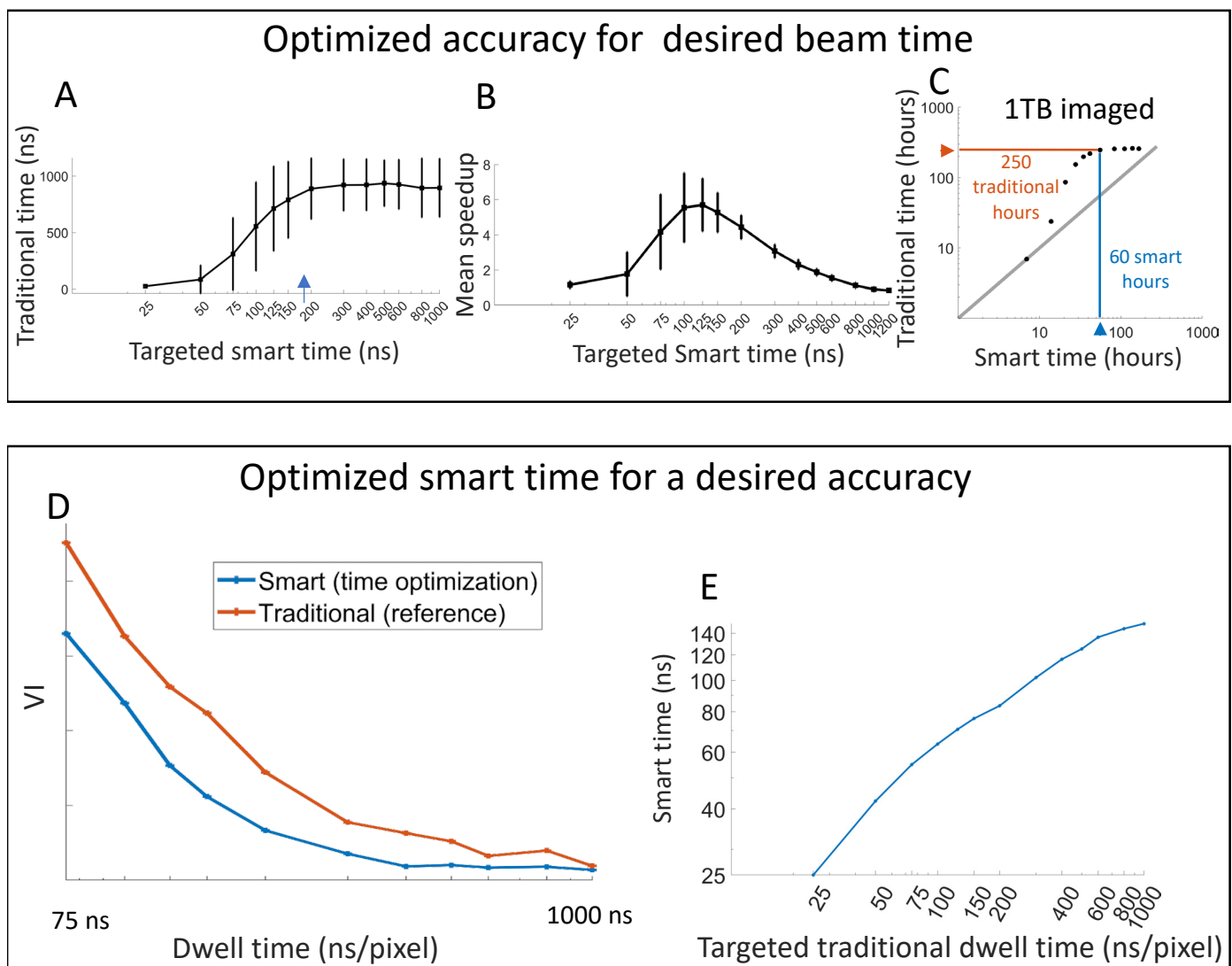


Figure 5. SmartEM acquisition time. In the first imaging scenario **A-C**, the imaging time is constrained by a time budget, which for a fixed volume and pixel resolution, provides the average dwell time (beam time). The task is to intelligently determine the SmartEM parameters that optimize segmentation accuracy. **A** For every targeted smart time (effective dwell time) the smartEM parameters that optimize segmentation accuracy are determined, including the standard (homogeneous) dwell time achieving that segmentation accuracy (y-axis). The longer the smart time is, the longer homogenous time is needed to achieve the same accuracy, with an asymptote around smart dwell time of 200 ns/pixel, equivalent to a homogeneous dwell time of about 800 ns/pixel. Error bars represent 1 s.d. **B** The speed up of the curve in **A**. The maximal speed up is achieved around the inflection point in **A**, around 125 ns/pixel - longer smart imaging up to 200 ns/pixel will still improve segmentation accuracy but with smaller speed up. **C** The data in **A** and **B** is shown for a fixed volume of 1 TB at 4nm per pixel and a slice thickness of 30 nm. **D** The variation of information of SmartEM compared to slowEM is calculated for each effective dwell time by optimizing the pipeline's parameters and the average VI across tiles is depicted. This allow calculating the two dwell times in the SmartEM (blue) versus standard (red) settings that produce the same accuracy (on average and per tile). **E** In the second imaging scenario, the quality of the EM is set in advance in terms of a desired dwell time of a standard pipeline, and the task is to find smart EM parameters that would provide that quality in a minimal amount of imaging time per volume. Maximal information for segmentation is achieved with around 140 ns/pixel for SmartEM and with around 800-1000 ns/pixel for standard EM.

448 parameter settings and calculates the T_{initial} , $T_{\text{re-scan}}$ and α set-
 449 tings that produce maximal accuracy (minimal VI) compared
 450 to the segmentation of reference tiles, while guaranteeing the
 451 effective dwell time (see **Supplement**).

452 **Figure 5A** presents the results of parameter optimization
 453 for different effective dwell times (smart imaging time) and
 454 image tiles. This optimization links any effective dwell time
 455 (achieved by optimizing the VI for different T_{initial} , $T_{\text{re-scan}}$) to
 456 an accuracy-equivalent standard homogeneous dwell time. For
 457 example, an effective dwell time of 200 ns (blue arrow)
 458 attains the maximal quality using a specific set of initial,
 459 re-scan dwell times, and re-scan rates that are determined per
 460 tile. This quality is comparable to standard homogeneous scan

at 800 ns/pixel.

Figure 5B depicts the time saved by SmartEM compared to
 standard microscopy. For the mouse cortex dataset, the maxi-
 mal saving compared to standard EM is achieved when smart
 EM is used at an effective dwell time of ~ 125 ns/pixel, which
 corresponds to the inflection point in **Figure 5A**, leads to an
 accuracy akin to ~ 725 ns/pixel by the standard pipeline. This
 effective dwell time produces images with nearly maximal possible
 segmentation accuracy (**Figure 1**). **Figure 5C** estimates
 the time to replicate the accuracy of SmartEM using standard
 microscopy using 1TB of mouse cortex (where 1 Byte corre-
 sponds to 1 pixel at $4 \times 4 \times 30 \text{ nm}^3$). The SmartEM microscope
 running for 60 hours of continuous imaging achieves the same

474 quality as a standard pipeline running for 250 hours.

475 *Scenario 2: Minimizing imaging time with fixed image*
476 *quality* In the second scenario a certain volume needs to be
477 segmented, and SmartEM is asked to minimize imaging cost.
478 Imaging time is not determined in advance, but the quality
479 of the smart EM has to meet a quality standard. SmartEM
480 needs to acquire the volume in a way that leads to comparable
481 segmentation to standard EM but in significantly less time.

482 First, the operator determines the dwell time that is needed
483 to achieve a specific quality with standard homogeneous
484 scanning. This dwell time can be obtained from the SmartEM
485 pipeline estimate of a minimum homogeneous dwell time
486 (Figure 1). Once the image quality is effectively determined
487 by selecting a reference dwell time for uniform scanning,
488 SmartEM needs to acquire the volume in a way that leads to
489 comparable segmentation accuracy, but in considerably shorter
490 time.

491 To analyze the expected imaging time of SmartEM in the
492 mouse cortex dataset, we first segmented images taken at ho-
493 mogeneous dwell times from 25 to 1200 ns uniform dwell times
494 from the same areas. We did the same for each image and each
495 effective dwell time, where each effective dwell time is derived
496 from the maximally accurate parameter set of initial and re-scan
497 dwell times and re-scan rate (Figure 5D). In all experiments
498 we used the same error detector (ERRNET) and the same neu-
499 ral network model to predict membrane from composite images
500 (FUSEDEM2MB). To match each standard homogeneous dwell
501 time to an effective smart dwell time, we calculated the shortest
502 smart dwell time that produces segmentation that is statistically
503 indistinguishable from the standard dwell time across tiles (see
504 Supplement). Figure 5E depicts the relation between the tar-
505 geted standard dwell time and the smart time that yields the
506 same accuracy. The highest possible quality of standard EM
507 at 1000 ns/pixel (see Figure 1) is attained by a smart effec-
508 tive dwell time of ~ 140 ns/pixel. This $\sim 7.1\times$ speed-up from
509 standard to SmartEM is achieved by selecting the percentage
510 of re-scanned pixels in each image tile, and letting ERRNET
511 determine re-scan locations.

512 In Figure S9 we tested the speed-up achieved by SmartEM
513 when re-scan rates are fixed in advance and only one pair of
514 initial and re-scan dwell times are used for imaging. These con-
515 straints allow direct comparison of the initial and re-scan dwell
516 times that optimize imaging time. As effective dwell time in-
517 creases, the time spent on re-scan also increases – the longest
518 dwell time for re-scan, with the equivalent segmentation accu-
519 racy as uniform dwell time (at 800 ns), is 1000 ns (initial dwell
520 time at 200 ns and effective dwell time at 300 ns). Efficiently
521 correcting errors in comparison to standard imaging with slower
522 dwell times also requires slower re-scan rates. Maximally slow
523 re-scan dwell times can be needed even when producing sub-
524 optimal segmentation (i.e. faster than 800-1000 ns of homo-
525 geneous dwell time). A re-scan dwell time of $2\text{-}3\times$ longer than the
526 homogeneous dwell time can yield optimal speed up. As the ef-
527 fective dwell time is allowed to exceed 500 ns and come closer
528 to the homogeneous dwell time, SmartEM no longer requires a
529 specific value for the initial scan dwell time (blue curve in Fig-
530 ure S9) which becomes an arbitrary choice while the re-scan

531 rate is maximal and only the percentage of re-scan is increased
532 to correct remaining errors.

533 Image acquisition with widely available point-scanning
534 SEM is now a limiting factor in connectomics. This evaluation
535 indicates that the SmartEM pipeline can yield $>7\times$ speed up
536 compared to standard image acquisition with a point-scanning
537 SEM without compromising quality and, at standard fast
538 acquisition (75ns-200ns), smartEM offers better quality.

539 Imaging mouse cortex with SmartEM

540 Figure 6 shows the outcome of SmartEM. A volume of size
541 $60\times 68\times 3\ \mu\text{m}^3$ (Figure 6A) and a section size $205\times 180\ \mu\text{m}^2$
542 was imaged at 4 nm pixel resolution. For volume acquisition,
543 we used an initial dwell time of 75 ns/pixel, re-scan of 800
544 ns/pixel, and re-scan rate of 10% providing an effective dwell
545 time of

$$\text{Effective dwell time} = 75 + 0.1 \cdot 800 = 155 \text{ ns/pixel.}$$

546 With optimal settings, this average dwell time will corre-
547 spond to a standard dwell time of ~ 1000 ns. To test the pipeline
548 on larger sections, we acquired a $205\times 180\ \mu\text{m}^2$ composed
549 of 30×30 individual tiles with the same pixel resolution. For
550 the SmartEM parameters, we used an initial dwell time of 75
551 ns/pixel and a rescan of 600 ns/pixel and a rescan rate of 10%
552 providing an effective dwell time of

$$\text{Effective dwell time} = 75 + 0.1 \cdot 600 = 135 \text{ ns/pixel.}$$

553 As mentioned above, this effective dwell time corresponds
554 to the maximal possible speed up of SmartEM for this dataset,
555 producing images with segmentation quality akin to standard
556 EM at ~ 1000 ns/pixel. We depict the segmentation of pipeline
557 outputs in Figure 6B, 6C, 6D using segmentation code that was
558 deployed on the microscope's support computer using exist-
559 ing tools (Pavarino et al., 2023). This 2-dimensional segmen-
560 tation can be used as input to a 3D-dimensional agglomeration
561 algorithm (Karlupia et al., 2023) to produce high quality
562 3-dimensional neuron reconstruction.

563 We also assessed the ability to detect synapses on short
564 dwell time images (from 25 ns to 1000 ns) and applied this
565 detection to the above initial scan of 75 ns/pixel with excellent
566 results that are comparable to slow scan imaging as shown in
567 Figure 6E, 6F, S7. In Figure 6G, 6H we show the ability
568 of SmartEM to detect and exclude regions of no interest,
569 where cytoplasm far from membrane is detected from initial
570 scan, allowing SmartEM to force the skipping of the long
571 dwell time scanning from these regions. In Figure 6I, 6J, S8
572 we demonstrate the ability to translate the fused images to a
573 uniform looking EM tiles with quality akin to long dwell time
574 imaging.

575 Discussion

576 The future and flexibility of SmartEM

577 Data analysis for connectomics is rapidly becoming faster,
578 easier, and cheaper thanks to rapid improvements in machine-
579 learning and the broadening availability of cloud-based tools

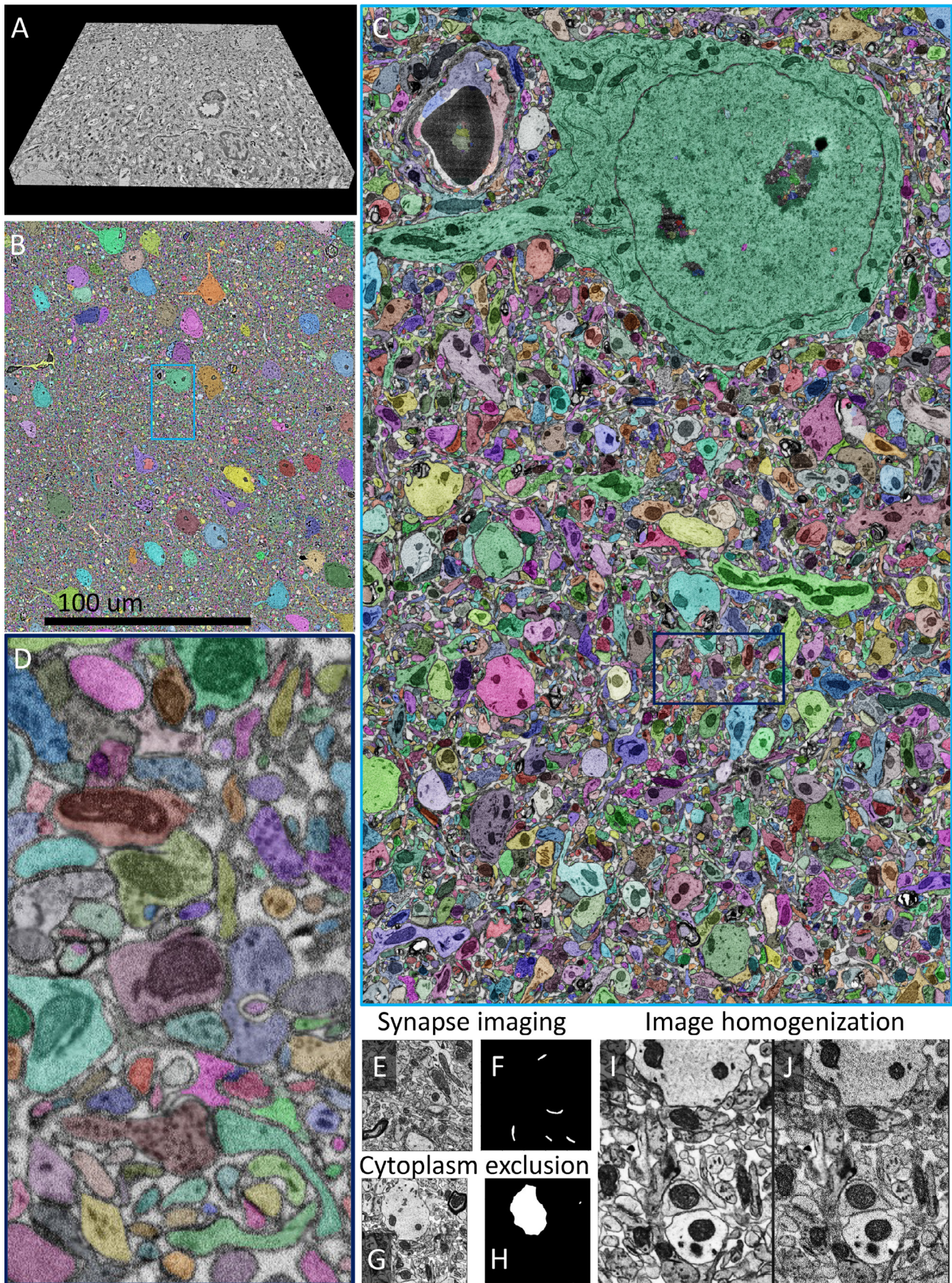


Figure 6. Segmentation of a mouse cortex volume using SmartEM. **A.** Stitched and aligned SmartEM volume of size $60 \times 68 \times 3 \mu\text{m}^3$. **B.** Segmentation of SmartEM volume using FUSEDEM2MB and watershed transform. **C.** Location of the highlighted region in B with respect to the total volume. **D.** Detailed depiction of segmentation in the boxed region in B (rotated). **E,F.** Automatic detection of synapses from short dwell time images. **G,H.** Automatic detection of regions to be excluded from short dwell time images. **I,J.** Images stylized from composite dwell times to appear akin to homogeneous dwell times.

580 and computational power. Data acquisition speed is now
581 becoming a bottleneck, rate-limited by the availability and
582 speed of microscope hardware. High-throughput electron
583 microscopes, like the Zeiss multibeam SEM, are not commonly
584 available. This SmartEM pipeline – because it is entirely
585 implemented in accessory computer hardware – can make
586 existing, widely available point-scanning SEMs usable for
587 connectomics with modest cost and modification.

588 The implementation of the three tools of the SmartEM
589 pipeline are designed so they can be altered depending on use
590 case from user to user or preparation to preparation.

591 **Tool 1** allows an SEM to identify error-prone regions in any
592 rapidly acquired image, but this concept can be implemented
593 with different underlying component algorithms. As described
594 above, **Tool 1** is built by training the ERRNET neural network
595 to detect error-prone regions on the basis of segmentation dif-
596 ferences that arise with fast and slow dwell times. Training the
597 ERRNET network allows a choice about what segmentation al-
598 gorithm to use to train the network. We used our recently devel-
599 oped two-dimensional segmentation algorithm (Pavarino et al.,
600 2023; Karlupia et al., 2023), but different laboratories will likely
601 have their own preferred segmentation algorithms. ERRNET
602 can be trained with any reliable segmentation algorithm. Be-
603 cause ERRNET is trained before image acquisition, the speed
604 or performance of the segmentation algorithm used to train ER-
605 RNET has no effect on pipeline performance. **Tool 2** allows
606 an SEM to perform the slow re-scan of any region within an
607 initially rapidly acquired image in real-time during microscope
608 operation. This slow scan can be done with any point-scanning
609 SEM with electrostatic scan generators that deflect the electron
610 beam to any pixel in an image much faster than the fastest dwell
611 time per pixel (>25 ns) (Mohammed and Abdullah, 2018; An-
612 derson et al., 2013). Electrostatic scan generators are common
613 to modern SEM systems built by most manufacturers. **Tool 3**
614 that performs segmentation of multi-dwell time images is used
615 off-line after image acquisition. The method that we imple-
616 mented to train Fused2MB can be extended to other segmen-
617 tation algorithms that work with fixed dwell times. Users could
618 adapt their own segmentation algorithms to work with the multi-
619 dwell time images that emerge from the SmartEM pipeline.

620 Diverse use cases for SmartEM

621 The underlying concept of SmartEM with a point-scanning
622 SEM can improve the efficiency and accuracy of image acqui-
623 sition in any context where it makes sense to adapt the time
624 spent on different regions, much like the human eye, which
625 rapidly captures most of a visual scene with low-resolution
626 (non-foveal) imaging and dwells on selected parts of the visual
627 image to remove ambiguity with high-resolution (foveal)
628 imaging (Thorpe et al., 1996). Point-scanning SEM is used in
629 materials science and manufacturing to assess samples that vary
630 in the spatial density of information content. Any application
631 where regions of high information content can be predicted (but
632 not accurately reconstructed) with an initial rapidly acquired
633 image can benefit from immediate re-scan of those regions,
634 guided by our SmartEM approach. Imaging approaches that
635 take advantage of electron beam sensitive materials, such

as cryo-EM would benefit from the selective re-scanning of
SmartEM. The objects of interest that are sparsely distributed
in the specimen, such as a specific mixture of molecules, will
be identified from the rapid initial scan and slowly re-scanned.

Here, we focused on re-scanning for connectomics to
capture information in error-prone regions with respect to
neuronal segmentation. But re-scanning could also be used
to capture information that is salient in other ways. As
we showed, we can also perform re-scanning to selectively
capture high-quality images of every chemical synapse in a
connectome, thereby providing high-quality morphological
reconstructions of salient structures in an image volume in
addition to resolving the problem of error-prone regions, while
still providing substantial pipeline speedup. SmartEM can be
adapted to other applications in cell biology or pathology by
recognizing and re-scanning other sparse cellular structures of
interest (e.g., mitochondria and other organelles).

The SmartEM pipeline can not only be “taught” to capture
the most salient features of an image, but can also be used to
neglect regions without interest. In most connectomics of larger
brains, nearly all objects in the field of view will be neural struc-
tures. But in small invertebrates, neural tissue might constitute
only a small part of the field of view. The *C. elegans* nerve
ring (brain) is <10% of the total volume of the body, and wraps
around the pharynx. Any two-dimensional brain section of the
C. elegans nervous system will also include substantial non-
neural tissue. To date, connectomic datasets have been acquired
by carefully designating the region-of-interest for each image.
The SmartEM pipeline may simplify and speed image acquisi-
tion by allowing the microscope to spend the time budget for
each image section on neurons instead of non-neuronal tissue
without needing the user to laboriously specify each region of
interest.

669 Adaptability of SmartEM for other microscopes and 670 other applications

Tape-based serial-section sample collection, where specimens
are stored permanently and can be re-imaged at any time, is
suited to SmartEM because any information that is lost dur-
ing imaging can be recovered. When specimens are imaged
for the purpose of connectomics, the SmartEM pipeline might
gloss over features that might eventually be of interest to other
scientists for other applications (e.g., cell biology). Because
serial-sections stored on tape can be safely archived for years,
they can be revisited at any time.

Instead of collecting serial sections on tape, one can use
block face imaging with serial tissue removal. One block face
approach, Focused Ion Beam SEM (FIB-SEM), has distinct ad-
vantages over tape-based serial-section sample collection, in-
cluding thinner tissue layers (4-8 nm) and better preservation of
image alignment (Knott et al., 2008). The principal disadvan-
tage of FIB-SEM has been the slow pace of traditional point-
scanning SEM with >1000 ns dwell times. This can be prob-
lematic when the microscope is used to collect extremely large
specimens, and must be continuously operational for days or
weeks without technical glitch. However, a FIB-SEM that im-
plements the SmartEM pipeline would be able to operate much

692 faster, increasing the likelihood of capturing an entire specimen
693 in single long runs. SmartEM is expected to provide greater
694 speed up on block face imaging because the imaging component
695 is a larger part of the entire acquisition pipeline compared to
696 serial-section SEM. Similar benefits will be obtained with other
697 block face imaging approaches such as Serial Block Face SEM
698 (SBF-SEM) where a diamond knife slices the specimen (Denk
699 and Horstmann, 2004). The downside of block face approaches,
700 whether with traditional imaging or the SmartEM pipeline, is
701 that each section is destroyed by ablation after being imaged,
702 forbidding revisiting the sample to capture any information that
703 was inadvertently lost.

704 **Improvements for SmartEM**

705 The performance of this software pipeline that runs in real-
706 time during microscope operation should improve further as
707 machine learning algorithms perform segmentation of rapidly
708 acquired images more accurately, a trend that can be expected
709 as more imaging is performed to generate training data for neural
710 networks and as neural networks themselves improve over
711 time. We expect gradual improvement in how rapid the initial
712 rapid image acquisition can be, and gradual improvement in
713 how many error-prone regions need to be re-scanned. A further
714 order-of-magnitude improvement in the SmartEM pipeline may
715 make point-scanning SEM systems comparably fast as more ex-
716 pensive multibeam systems. We note that current multibeam
717 SEM systems cannot be sped up with this SmartEM strategy,
718 because their multiple beams are coordinated and cannot be in-
719 dependently controlled, a fundamental requirement of this ap-
720 proach.

721 **Summary**

722 All components needed to implement the SmartEM pipeline
723 on the ThermoFisher Verios G4 UC will be provided as
724 open source software. The basic conceptual workflow of the
725 SmartEM pipeline is adaptable to other microscope platforms.

726 **Code Availability**

727 Machine learning software and all models will be made avail-
728 able upon publication and are currently available on request.

729 **Acknowledgements**

730 Research reported in this paper was supported by the NIH
731 BRAIN Initiative under award number 1U01NS132158 and by
732 NIH grants 5U24NS109102 and U01 NS108637. L.M.'s work
733 was supported in part by a fellowship from MathWorks.

734 **Declaration of Interests**

735 P.P., M.P. and R.S. are employees of Thermo Fisher Scientific.

References

- 736
- 737 Abbott, L.F., Bock, D.D., Callaway, E.M., Denk, W., Dulac, C., Fairhall, A.L., Fiete, I., Harris, K.M.,
738 Helmstaedter, M., Jain, V., et al. (2020). The mind of a mouse. *Cell* 182, 1372–1376.
- 739 Anderson, H.S., Ilic-Helms, J., Rohrer, B., Wheeler, J., and Larson, K. (2013). Sparse imaging for fast
740 electron microscopy. In *Computational Imaging XI* (International Society for Optics and Photonics),
741 vol. 8657, p. 86570C.
- 742 Beier, T., Pape, C., Rahaman, N., Prange, T., Berg, S., Bock, D.D., Cardona, A., Knott, G.W., Plaza,
743 S.M., Scheffer, L.K., et al. (2017). Multicut brings automated neurite segmentation closer to
744 human performance. *Nature methods* 14, 101–102.
- 745 Bidel, F., Meirovitch, Y., Schalek, R.L., Lu, X., Pavarino, E.C., Yang, F., Peleg, A., Wu, Y., Shomrat, T.,
746 Berger, D.R., et al. (2023). Connectomics of the *Octopus vulgaris* vertical lobe provides insight
747 into conserved and novel principles of a memory acquisition network. *eLife* 12.
- 748 Bock, D.D., Lee, W.C.A., Kerlin, A.M., Andermann, M.L., Hood, G., Wetzel, A.W., Yurgenson, S.,
749 Soucy, E.R., Kim, H.S., and Reid, R.C. (2011). Network anatomy and in vivo physiology of visual
750 cortical neurons. *Nature* 471, 177–182.
- 751 Denk, W., and Horstmann, H. (2004). Serial block-face scanning electron microscopy to reconstruct
752 three-dimensional tissue nanostructure. *PLoS biology* 2, e329.
- 753 Fang, L., Monroe, F., Novak, S.W., Kirk, L., Schiavon, C.R., Yu, S.B., Zhang, T., Wu, M., Kastner, K.,
754 Latif, A.A., et al. (2021). Deep learning-based point-scanning super-resolution imaging. *Nature*
755 *Methods* 18, 406–416.
- 756 Hayworth, K.J., Morgan, J.L., Schalek, R., Berger, D.R., Hildebrand, D.G.C., and Lichtman, J.W.
757 (2014). Imaging atom ultrathin section libraries with wafermapper: a multi-scale approach to em
758 reconstruction of neural circuits. *Frontiers in Neural Circuits* 8, 68–68.
- 759 He, K., Zhang, X., Ren, S., and Sun, J. (2016). Deep residual learning for image recognition. In 2016
760 IEEE Conference on Computer Vision and Pattern Recognition (CVPR). pp. 770–778.
- 761 Hildebrand, D.G.C., Cicconet, M., Torres, R.M., Choi, W., Quan, T.M., Moon, J., Wetzel, A.W.,
762 Scott Champion, A., Graham, B.J., Randlett, O., et al. (2017). Whole-brain serial-section electron
763 microscopy in larval zebrafish. *Nature* 545, 345–349.
- 764 Ioffe, S., and Szegedy, C. (2015). Batch normalization: Accelerating deep network training by reducing
765 internal covariate shift. In *Proceedings of the 32nd International Conference on Machine Learning*,
766 F. Bach, and D. Blei, eds. (Lille, France: PMLR), *Proceedings of Machine Learning Research*,
767 vol. 37, pp. 448–456. <https://proceedings.mlr.press/v37/ioffe15.html>.
- 768 Isola, P., Zhu, J.Y., Zhou, T., and Efros, A.A. (2016). Image-to-image translation with conditional
769 adversarial networks .
- 770 Januszewski, M., Kornfeld, J., Li, P.H., Pope, A., Blakely, T., Lindsey, L., Maitin-Shepard, J., Tyka, M.,
771 Denk, W., and Jain, V. (2018). High-precision automated reconstruction of neurons with flood-
772 filling networks. *Nature methods* 15, 605–610.
- 773 Karlupia, N., Schalek, R.L., Wu, Y., Meirovitch, Y., Wei, D., Charney, A.W., Kopell, B.H., and Licht-
774 man, J.W. (2023). Immersion fixation and staining of multicubic millimeter volumes for electron
775 microscopy-based connectomics of human brain biopsies. *Biological Psychiatry* .
- 776 Kasthuri, N., Hayworth, K., Berger, D., Schalek, R., Conchello, J., Knowles-Barley, S., Lee, D.,
777 Vázquez-Reina, A., Kaynig, V., Jones, T., et al. (2015). Saturated reconstruction of a volume
778 of neocortex. *Cell* 162, 648–661.
- 779 Kingma, D.P., and Ba, J. (2014). Adam: A method for stochastic optimization .
- 780 Knott, G., Marchman, H., Wall, D., and Lich, B. (2008). Serial section scanning electron microscopy of
781 adult brain tissue using focused ion beam milling. *The Journal of Neuroscience* 28, 2959–2964.
- 782 Kornfeld, J., Januszewski, M., Schubert, P., Jain, V., Denk, W., and Fee, M.S. (2020). An anatomical
783 substrate of credit assignment in reinforcement learning. *BioRxiv* pp. 2020–02.
- 784 Li, Y., Meirovitch, Y., Kuan, A.T., Phelps, J.S., Pacureanu, A., Lee, W.C.A., Shavit, N., and Mi, L.
785 (2023). X-ray2em: Uncertainty-aware cross-modality image reconstruction from x-ray to electron
786 microscopy in connectomics. *ArXiv.org* .
- 787 Lichtman, J.W., Pfister, H., and Shavit, N. (2014). The big data challenges of connectomics. *Nature*
788 *neuroscience* 17, 1448–1454.
- 789 Lomba, S., Strahle, J., Gangadharan, V., Heike, N., Khalifa, A., Motta, A., Meyer, H.S., Helmstädter,
790 M., and Sievers, M. (2022). Connectomic comparison of mouse and human cortex. *Science* 377,
791 171–+.
- 792 Lu, X., Wu, Y., Schalek, R.L., Meirovitch, Y., Berger, D.R., and Lichtman, J.W. (2023). A scalable
793 staining strategy for whole-brain connectomics. *bioRxiv* pp. 2023–09.
- 794 Meila, M. (2003). Comparing clusterings by the variation of information. In *Learning Theory and*
795 *Kernel Machines* (Berlin, Heidelberg: Springer Berlin Heidelberg), *Lecture Notes in Computer*
796 *Science*, vol. 2777, pp. 173–187.
- 797 Meirovitch, Y., Mi, L., Saribekyan, H., Matveev, A., Rolnick, D., and Shavit, N. (2019). Cross-
798 classification clustering: An efficient multi-object tracking technique for 3-d instance segmentation
799 in connectomics. In *Proceedings of the IEEE/CVF Conference on Computer Vision and Pattern*
800 *Recognition*. pp. 8425–8435.
- 801 Mi, L., Wang, H., Meirovitch, Y., Schalek, R., Turaga, S.C., Lichtman, J.W., Samuel, A.D.T., and Shavit,
802 N. (2021). Learning guided electron microscopy with active acquisition. *Medical Image Computing*
803 *and Computer Assisted Intervention* pp. 77–87.
- 804 Minnen, D., Januszewski, M., Blakely, T., Shapson-Coe, A., Schalek, R.L., Ballé, J., Lichtman, J.W.,
805 and Jain, V. (2021). Denoising-based image compression for connectomics. *bioRxiv* .
- 806 Mirza, M., and Osindero, S. (2014). Conditional generative adversarial nets .
- 807 Mohammed, A., and Abdullah, A. (2018). Scanning electron microscopy (sem): A review. In *Pro-*
808 *ceedings of the 2018 International Conference on Hydraulics and Pneumatics—HERVEX, Băile*
809 *Govora, Romania*. vol. 2018, pp. 7–9.
- 810 Morgan, J.L., Berger, D.R., Wetzel, A.W., and Lichtman, J.W. (2016). The fuzzy logic of network
811 connectivity in mouse visual thalamus. *Cell* 165, 192–206.
- 812 Paszke, A., Gross, S., Massa, F., Lerer, A., Bradbury, J., Chanan, G., Killeen, T., Lin, Z., Gimelshein,
813 N., Antiga, L., et al. (2019). Pytorch: An imperative style, high-performance deep learning library
814 .
- 815 Pavarino, E.C., Yang, E., Dhanyasi, N., Wang, M.D., Bidel, F., Lu, X., Yang, F., Francisco Park, C.,
816 Bangalore Renuka, M., Drescher, B., et al. (2023). membrain: an interactive deep learning matlab
817 tool for connectomic segmentation on commodity desktops. *Frontiers in Neural Circuits* 17.
- 818 Pizer, S., Johnston, R., Ericksen, J., Yankaskas, B., and Muller, K. (1990). Contrast-limited adaptive
819 histogram equalization: speed and effectiveness. In [1990] *Proceedings of the First Conference*
820 *on Visualization in Biomedical Computing* (IEEE Comput. Soc. Press), pp. 337–345.
- Potocek, P. (2021). Adaptive specimen image acquisition using an artificial neural network. US Patent
10,928,335.
- Ronneberger, O., Fischer, P., and Brox, T. (2015). U-net: Convolutional networks for biomedical image
segmentation. In *International Conference on Medical image computing and computer-assisted*
intervention (Springer), pp. 234–241.
- Saalfeld, S., Fetter, R., Cardona, A., and Tomancak, P. (2012). Elastic volume reconstruction from
series of ultra-thin micrographs sections. *Nature Methods* 9, 717–U280.
- Shapson-Coe, A., Januszewski, M., Berger, D.R., Pope, A., Wu, Y., Blakely, T., Schalek, R.L., Li,
P., Wang, S., Maitin-Shepard, J., et al. (2021). A connectomic study of a petascale fragment of
human cerebral cortex. *bioRxiv* .
- Shavit, N., Samuel, A., Lichtman, J., and Mi, L. (2021). System and method for learning-guided
electron microscopy. US Patent 11,164,721.
- Shavit, N., Samuel, A., Lichtman, J., and Mi, L. (2023). System and method for learning-guided
electron microscopy. US Patent 11,557,459.
- Sheridan, A., Nguyen, T.M., Deb, D., Lee, W.C.A., Saalfeld, S., Turaga, S.C., Manor, U., and Funke, J.
(2023). Local shape descriptors for neuron segmentation. *Nature Methods* 20, 295–303.
- Song, K., Feng, Z., and Helmstaedter, M. (2023). High-contrast en bloc staining of mouse whole-brain
and human brain samples for em-based connectomics. *Nature Methods* 20, 836–840.
- Swanson, L.W., and Lichtman, J.W. (2016). From cajal to connectome and beyond. *Annual Review*
of *Neuroscience* 39, 197–216.
- Thermo Fisher Scientific (2018). Software SEM and FIB SEM software for Python-based
scripting control of your instrument. Available at <https://www.thermofisher.com/cz/en/home/electron-microscopy/products/software-em-3d-vis/autoscript-4-software.html>, AutoScript 4.
- Thermo Fisher Scientific (2020). Verios 5 XHR SEM. Scanning electron microscopy
characterization of nanomaterials with sub-nanometer resolution and high material con-
trast. Available at <https://www.thermofisher.com/us/en/home/electron-microscopy/products/scanning-electron-microscopes/verios-xhr-sem.html>.
- Thorpe, S., Fize, D., and Marlot, C. (1996). Speed of processing in the human visual system. *nature*
381, 520.
- Vincent, L., and Soille, P. (1991). Watersheds in digital spaces: an efficient algorithm based on
immersion simulations. *IEEE Transactions on Pattern Analysis & Machine Intelligence* 13, 583–
598.
- Wang, H., Rivenson, Y., Jin, Y., Wei, Z., Gao, R., Gunaydin, H., Bentolila, L.A., Kural, C., and Ozcan,
A. (2019). Deep learning enables cross-modality super-resolution in fluorescence microscopy.
Nature Methods 16, 103–110.
- Weigert, M., Schmidt, U., Boothe, T., Mueller, A., Dibrov, A., Jain, A., Wilhelm, B., Schmidt, D.,
Broaddus, C., Culley, S., et al. (2018). Content-aware image restoration: pushing the limits of
fluorescence microscopy. *Nature Methods* 15, 1090–1097.
- White, J.G., Southgate, E., Thomson, J.N., and Brenner, S. (1986). The structure of the nervous
system of the nematode *Caenorhabditis elegans*. *Philosophical Transactions of the Royal Society*
B: *Biological Sciences* 314, 1–340.
- Witvliet, D., Mulcahy, B., Mitchell, J.K., Meirovitch, Y., Berger, D.R., Wu, Y., Liu, Y., Koh, W.X., Par-
vathala, R., Holmyard, D., et al. (2021). Connectomes across development reveal principles of
brain maturation. *Nature* 596, 257–261.
- Xu, C.S., Januszewski, M., Lu, Z., Takemura, S.y., Hayworth, K.J., Huang, G., Shinomiya, K., Maitin-
Shepard, J., Ackerman, D., Berg, S., et al. (2020). A Connectome of the Adult *Drosophila* Central
Brain. *bioRxiv* .

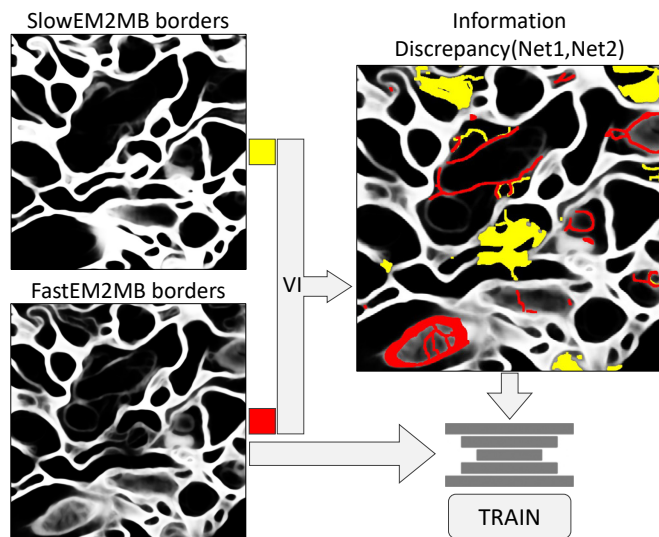


Figure S1. The discrepancy between segmentation with long dwell time (using SLOWEM2MB) and short dwell time (using FASTEM2MB) is defined based on VI. VI is the sum of individual error terms contributed by each object in the two segmented images. The most variable objects are flagged. Image processing is used to delineate specific borders that appear in only one segmented image. Yellow represents segmented objects that are uniquely predicted in the long dwell time image. Red represents segmented objects that are uniquely predicted in the short dwell time image. A neural network (ERRNET) is trained to predict all red and yellow discrepancies only using short dwell time images. This is possible because variation occurs where membrane predictors are uncertain and often with typical, at times biologically implausible, membrane prediction.

Supplemental Information

Segmenting composite images

The smart microscope should be able to analyze images composed from multiple dwell times (see **Figures 1C, 2B, 2C, 4A, 6A-6D**). We tested whether replacing error-prone regions in a short dwell time image with regions taken from long dwell time images improves segmentation outcomes. **Figure S2** depicts the segmentation outcome of a short dwell time image taken at 100 ns/pixel segmented with a dedicated 100 ns network FASTEM2MB (**S2A,S2E**), and by FUSEDEM2MB (**S2B,S2F**). The segmentation quality of these networks are similar (top panel; VI=0.025 and VI=0.022). In most scenarios, the network trained to deal with fused EM (FUSEDEM2MB) produces better results than networks trained to handle a fixed dwell time, even if the input to the two networks consists of a single homogeneous dwell time. **Figures S2C, S2G** depict the segmentation of an image where the error-prone regions were detected by an error detector and replaced with long dwell time pixels (2500 ns). The error level is typically and substantially cut by $\sim 3-4 \times$. The 2500 ns reference image and its segmentation are shown in **Figures S2D, S2H**. All error estimates based on VI shown in **Figure S2** are presented as the sum of the merge error term and split error term.

Imaging procedure

The SEM is automated to acquire images of individual tiles of every specimen section that are eventually stitched and aligned to form a total image volume **Figure 4**. The microscope navigates through multiple specimen sections held on tape and defines every specimen region of interest (S-ROI). Each S-ROI

is captured at high spatial resolution by multi-tile acquisition. To identify the S-ROI and automate stage position and rotation control, we used SEM Navigator, a custom interface akin to earlier WaferMapper software (**Hayworth et al., 2014**). The list of S-ROIs is exported into a text file, which is subsequently processed by the SmartEM pipeline (coded in Python/Matlab) using the Thermo Fisher Scientific Autoscript (**Thermo Fisher Scientific, 2018**) package. The SmartEM pipeline controls the Verios (**Thermo Fisher Scientific, 2020**) microscope, moves to S-ROI and individual tile positions, controlling the entire acquisition sequence.

For all image acquisitions, we used the Verios UHR (Ultra High Resolution) imaging mode with 4nm/pixel spatial resolution and ~ 4 mm working distance. Image contrast was obtained using a back-scattered electron detector with 2000 V stage bias. The initial short dwell time scan was obtained using the full frame acquisition Autoscript interface. The subsequent long dwell time re-scan utilized the standard interface of Autoscript patterning

To optimize image quality and tuning time for both short movements between neighboring tiles and long movements neighboring sections, we customized sequences of various autofunctions. These autofunctions included auto-contrast/brightness (ACB), auto-focus (AF), auto-stigmation (AS), auto-focus/stigmation (AFS), and auto-lens (AL) alignment.

Because we used different interfaces for the initial short dwell time scan and long dwell time re-scan, an additional alignment procedure was necessary to achieve pixel-resolution precision in the re-scan. The basic system configuration for the re-scan acquisition is described in **Potocek (2021)**.

When the re-scan long dwell time was shorter than ~ 500 ns/pixel, an unavoidable artifact due to limited system response of the electron deflection system occurred at the edge of re-scan regions. We excised this artifact by omitting a 1-pixel boundary from every re-scan region.

Segmentation quality metric

To compare the segmentation quality of different samples we used a variation of information (VI) metric (**Meila, 2003**). In principle all comparisons that we made in this study can be accomplished with other metrics of segmentation quality as long as they can be applied to 2-dimensional images. We expect the choice of segmentation metric to have little effect as long as any metric assesses similar topological attributes as VI (i.e., whether objects are split or merged). Our implementation of the VI running on CPU/GPU is available at <https://pypi.org/project/python-voi/>.

Using VI to build ERRNET. To train the error detectors we needed to locate the specific regions that contribute to the largest segmentation differences between image pairs, which is not provided by the VI metric. VI combines split and merge errors. The two error measures are defined by comparing the entropy of three segmented images (**Meila, 2003**), $S_1 \in L_1^N$, $S_2 \in L_2^N$ and $S_1 \times S_2 \in L_1^N \times L_2^N$ for two N -pixel labeling (instance segmentation) S_1 and S_2 that needs to be compared, where the L_s represents the sets of pixel labels. The segmented

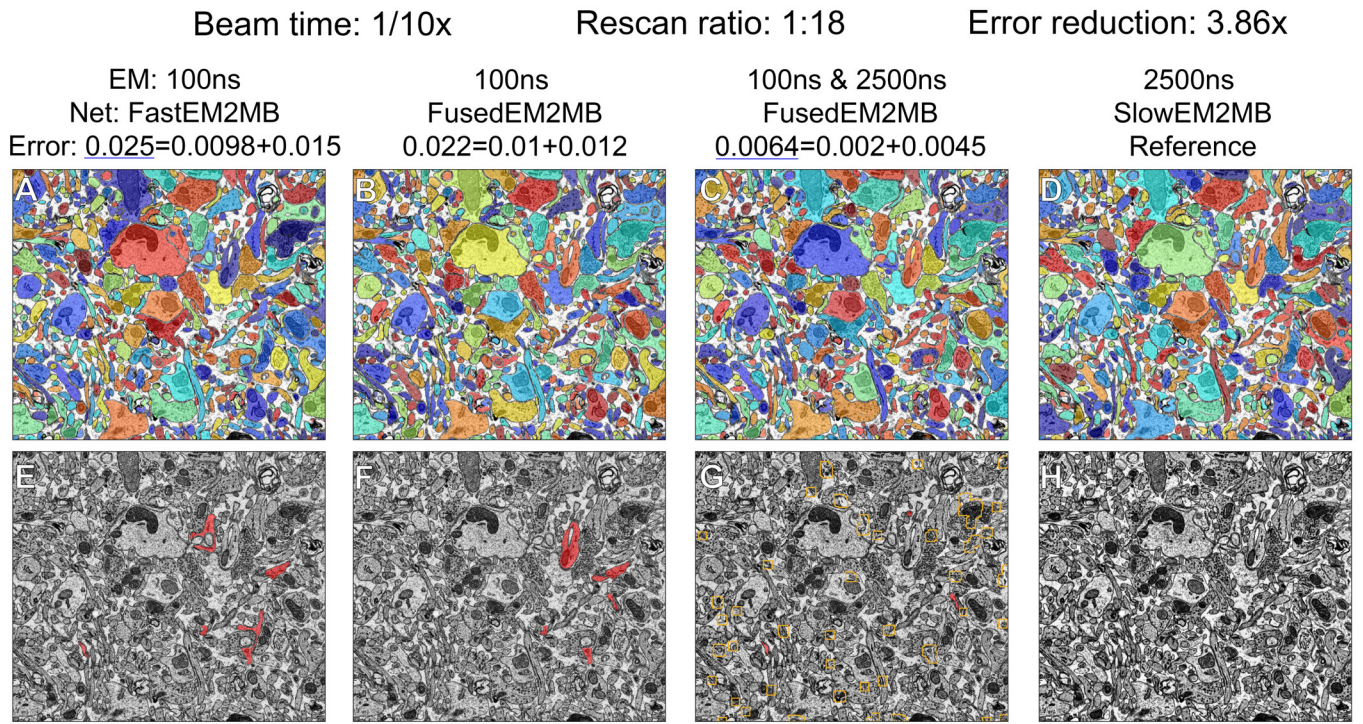


Figure S2. Composite EM images fusing short and a long dwell time regions are better segmented compared to short dwell time images. We tested whether replacing error-prone regions harms the ability to segment. Composite images tend to be segmented with dramatically higher accuracy.

953 image $S_1 \times S_2$ is labeled by concatenating the labels from S_1
 954 and S_2 for each pixel. The VI is then the sum of two error
 955 terms VI_{merge} and VI_{split}

$$\begin{aligned} VI_{\text{merge}} &= H(S_1 \times S_2) - H(S_1), \\ VI_{\text{split}} &= H(S_1 \times S_2) - H(S_2), \\ VI &= VI_{\text{merge}} + VI_{\text{split}}. \end{aligned} \quad (1)$$

956 Due to the additivity of the entropy measure (Meila, 2003),
 957 VI_{merge} and VI_{split} can be broken into individual constituents,
 958 representing the amount of error contributed by each individ-
 959 ual label in each segmentation. We could thus rank objects in
 960 each segmentation according to the amount of variation they
 961 contribute to overall VI (Figures S5). The error contributed by
 962 the set of pixels that are both in segment $s_1 \in S_1$ and $s_2 \in S_2$
 963 (i.e. the error contributed by a segment in $S_1 \times S_2$) is

$$W(s_1 \cap s_2) - W(s_1)$$

964 and

$$W(s_1 \cap s_2) - W(s_2),$$

965 for the split and merge errors, respectively, where $W(A) =$
 966 $-\frac{|A|}{N} \cdot \log \frac{|A|}{N}$, $|A|$ is the number of pixels in A and N is the
 967 number of pixels in the image.

968 Once the significantly incompatible objects are detected in
 969 each segmentation, we used image processing to delineate the
 970 borders that are responsible for the topological differences be-
 971 tween the two segmented images (Figure S1). We then pro-
 972 duced binary masks from these errors and trained neural net-

works (ERRNET) to detect them directly from membrane prob- 973
 ability maps, themselves produced by another neural network 974
 (FASTEM2MB). Detecting borders allows our technique to dis- 975
 regard small “cosmetic” variations between two segmentations 976
 that do not cause meaningful topological differences. 977

Determination of maximal segmentation quality. We developed 978
 an unbiased estimate for the minimal dwell needed for 2D seg- 979
 mentation. We compared segmentations from N images for 980
 each pair of dwell times $d_1 < d_2$ and an overly slow dwell 981
 time d_{ref} . We asked whether the VI of the d_2 images was sig- 982
 nificantly smaller ($p < 0.05$) than d_1 images compared to d_{ref} 983
 images. When two dwell times were not sufficiently different, 984
 we call these dwell times equivalent. We defined the minimum 985
 dwell time with near maximal segmentation ability as that dwell 986
 time beyond which VI does not improve. 987

Forcing fast scan imaging of desired regions 988

The acceleration of SmartEM depends on the quantity of 989
 re-scanned pixels. Since the re-scanning mask is learned rather 990
 than calculated through a fixed process, regions irrelevant to 991
 the connectomics task may contain error-prone regions and 992
 appear in the re-scan map, potentially reducing speedup. To 993
 exclude irrelevant regions from slow re-scan, we built another 994
 neural network module (MUSTEXCLUDE) to calculate what 995
 regions should be excluded from any re-scan, even if they 996
 might be flagged as error-prone by ERRNET. Developing a 997
 separate MUSTEXCLUDE module (rather than adding this 998
 capability to ERRNET) conferred additional flexibility to the 999
 SmartEM pipeline by allowing us to adaptively choose what 1000
 regions should be excluded from re-scan without retraining 1001
 ERRNET. Bypassing irrelevant pixels (e.g., cell nuclei, blood 1002

vessels) during re-scan boosts efficiency by conserving time and computational resources.

Here, we implement MUSTEXCLUDE to exclude regions that are sufficiently far from any cellular membranes. To do this, we utilize the Euclidean distance transform on input binary membranes. This transform calculates the shortest Euclidean distance from each zero pixel (background) to any non-zero (foreground) pixel in the image. To train MUSTEXCLUDE, we binarize the distance transform with a fixed threshold (Figure S13). The features of irrelevant regions we learned as a semantic segmentation task using paired EM images and their binary masks (see **Neural network models**). The SmartEM pipeline applies MUSTEXCLUDE in real-time on short dwell time images and precludes re-scanning irrelevant regions that might have been predicted by ERRNET. To assess the performance of different modules in the SmartEM pipeline, we exclude MUSTEXCLUDE from speedup tests shown in Figure 5. For the cytoplasm exclusion described above, the average exclusion proportion is about 23% as shown in Figure S13. The speedup tests shown in Figure 5 would improve with the implementation of MUSTEXCLUDE.

Identifying additional high-interest regions for slow re-scan

ERRNET identifies regions susceptible to segmentation errors and re-scans them at a higher quality to improve segmentation accuracy. The same strategy can be re-formulated, not only to identify error-prone regions, but to identify additional image-specific regions of special interest, such as synapses or any sub-cellular component of biological interest. Here, we built an additional neural network module (MUSTINCLUDE) to re-scan regions identified as synapses, because of their high relevance to connectomics. Mouse cortex typically contains ~ 1 -1.5 synapses per μm^3 (Kasthuri et al., 2015), or ~ 2 -3 synapses per field of view when image tiles are $\sim 8 \times 8 \mu\text{m}^2$. Because of synapse sparsity, the re-scan time does not substantially increase. We trained MUSTINCLUDE with a set of manually-annotated long dwell time SEM images.

To train MUSTINCLUDE, we first trained a neural network to detect synapses using manual annotations of long dwell time images (SYNAPSENET). The high performance of SYNAPSENET is shown in Figure S7. We paired short dwell time images with the binary masks for synapse locations predicted by SYNAPSENET (which had used long dwell time images to make the predictions). This procedure created ground truth to train MUSTINCLUDE. A snapshot of the synapse detection and re-scan mask generation pipeline is shown in Figure S11. The hyper-parameters and training details of MUSTINCLUDE are similar to MUSTEXCLUDE.

Optional image homogenization

The SmartEM pipeline produces composite image with pixels acquired at different dwell times. A human observer will note contrast differences at interfaces between pixels with different dwell times. To increase human image interpretability, we built an image translator component that homogenizes SmartEM images to look like standard EM images with uniform dwell times.

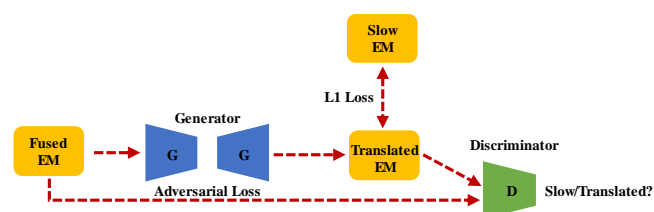


Figure S3. Image Translation Model. G: *generator*. D: *discriminator*. The generator takes a composite EM as input and produces a translated EM that looks similar to slow EM. The discriminator takes both composite EM and translated EM (or slow EM) as input and aims to distinguish translated from slow.

Figure S8 shows a specific example, a fused EM image that is a mosaic of sub-images with different dwell times. To mitigate dwell time contrasts and produce a visually coherent image, we applied a conditional generative adversarial network (IMAGE-HOMOGENIZER, cGANs) (Mirza and Osindero, 2014). Previous studies used deep learning to improve the quality of microscopy images (Fang et al., 2021; Wang et al., 2019; Weigert et al., 2018; Mi et al., 2021), de-noise EM images (Minnen et al., 2021), and perform image reconstruction across different modalities (Li et al., 2023). IMAGEHOMOGENIZER contains two convolutional neural networks (CNN): a *generator* and a *discriminator* (Isola et al., 2016). Training data are a composite image and a uniformly long dwell time image, where the composite image is generated by randomly combining pixels from short dwell time and long dwell time images in different proportions (Figures 6B,6C,6D where the composite images consist of 75 ns and 600 ns pixel dwell times). As shown in Figure S3, during the training process, the *generator* translates the simulated composite images to resemble long dwell time images, and the *discriminator* attempts to distinguish the translated images from real long dwell time images. The training process utilizes L1 loss and adversarial loss. After image homogenization by the *generator*, the fused EM images are more suitable for human inspection and retain the visual details of fine ultrastructure Figure S8.

Neural network architectures

For all neural network models, we strove for simple architectures that would allow straightforward reproducibility of results. A U-Net like architecture (Ronneberger et al., 2015) was used to train membrane detection of homogeneous dwell time EMs (SLOWEM2MB, FASTEM2MB), any dwell-time EM (EM2MB), and composite EM where each image fuses more than one dwell time (FUSEDEM2MB). We found that FUSEDEM2MB, once trained, could be used for all membrane prediction tasks without compromising quality. The same U-net architecture was also used to train ERRNET, SYNAPSENET, MUSTINCLUDE, and MUSTEXCLUDE. We tried the U-net architecture for image homogenization, but achieved better results with conditional GANs.

Architecture for FUSEDEM2MB and ERRNET. The selected architecture, similar to the UNET (Ronneberger et al., 2015), shown in Figure S14 has 3 sets of 2D-Convolution, Batch-Normalization (Ioffe and Szegedy, 2015), ReLU in each layer. We use residual connections (He et al., 2016) adding the output

of the first convolution to the last one in each layer. This architecture showed the highest segmentation accuracy when varying the number of CBR (Conv-BatchNorm-ReLU) in each layer (2~4), the usage of residual connections, and the type of residual connections (concatenation or addition).

U-Net architecture for MUSTEXCLUDE. We trained a fully convolutional UNET model over 200 epochs, employing a learning rate of 0.01. The model was configured with five layers of depth and filter sizes progressively sequenced as 32, 64, 128, 256, and 512. To introduce non-linearity and manage potential negative inputs, we incorporated a leakyReLU activation function.

Image Normalization and Augmentation. To train the FUSEDEM2MB network, we used the CLAHE (Pizer et al., 1990) normalization with $clipLimit=3$ to bring all images to a common color space. We used on the fly rotation, flip, translation to augment the images in the training set. Although images are naturally 2048×2048 , we sub-sampled 256×256 squares to train the network. To allow the network to deal with images with multiple dwell times, we randomly replace patches at random locations with different dwell times. Specifically, each sample was generated by choosing a baseline image at a single dwell time and replacing up to 30 patches with a maximum size of 11×11 pixels with the corresponding pixels of an image with longer dwell time.

To train ERRNET, we normalized membrane probabilities to $[0,1]$ as an input to the network. We used the same procedure for on the fly translation and rotation but did not replace patches.

Training Procedure. We used the Pytorch framework (Paszke et al., 2019) to implement and optimize the network. The Adam optimizer (Kingma and Ba, 2014) with learning rate 0.001 was used to update the network parameters. We used a batch size of 16 images. We trained the FUSEDEM2MB network for 50000 gradient steps. We evaluated validation loss every 1000 steps over 100 batches. The network converged after ~35000 gradient steps. The same procedure was used to train ERRNET. ERRNET converged after ~8000 gradient steps.

Image Translation Networks. IMAGEHOMOGENIZER uses a conditional GAN called pix2pix (Isola et al., 2016), consisting of a generator CNN and discriminator CNN. The generator includes an encoder and decoder that downsamples and then up-samples the input image. The discriminator tries to discriminate between slow EM and translated EM. At the training stage, we use a batch size of 1 and randomly crop 128×128 image tiles from a larger composite EM image. The model is first trained with a constant learning rate of 0.0002 for 100 epochs and then for another 100 epochs, during which the learning rate decays to zero. At the inference stage, the whole composite EM image is passed to the model without cropping.

Image stitching and alignment

The stitching and alignment of the sample volume was performed on composite dwell time images. After applying a band-pass filter to raw images, we used conventional block matching technique (Saalfeld et al., 2012) to obtain matching points between neighboring images, from which elastic transformations

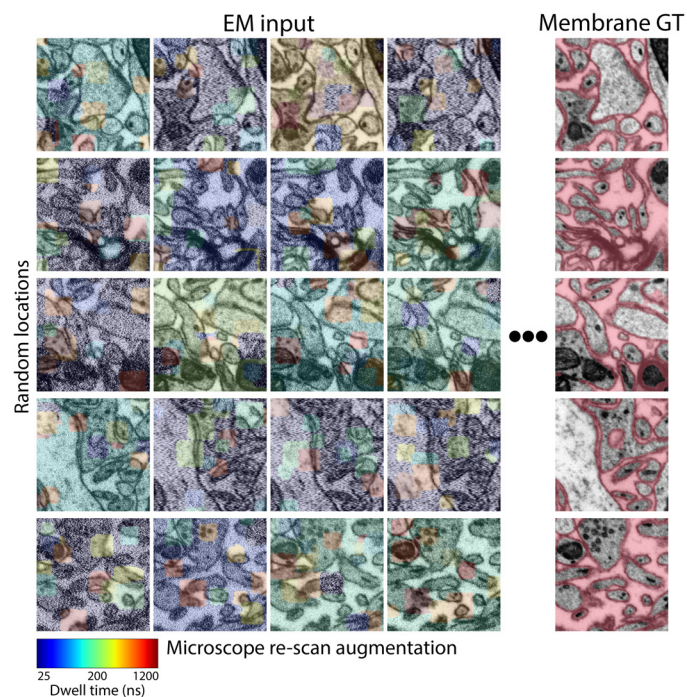


Figure S4. Dwell-time re-scan data augmentation. Rows 1-5 show different locations in the EM sample. Columns 1-4 show different augmented composite images that were taken at different dwell times; short dwell time pixels in blue, representing 25 ns scans; long dwell time pixels in red, representing 1200 ns pixels. Column 5 shows the groundtruth classes for each region that were obtained from the long dwell time neural network (SLOW2EM). The aim of FUSEDEM2MB is to classify membrane pixels. Additional augmentations such as translation, rotation, and flip are used during training.

mapping the raw data to the aligned volume were computed by mesh relaxation. Code for stitching and alignment is available at [Stitching and alignment code](#). We applied the same stitching and alignment transformations to the fast, composite, and homogenized images to produce three sets of final volumes.

Statistical tests

All statistical tests were done using the Wilcoxon signed-rank test for paired samples. The test was used to assess the cases where two dwell times produce similar segmentation quality by comparing the variation of information of individual samples to a single reference taken at a longer dwell time.

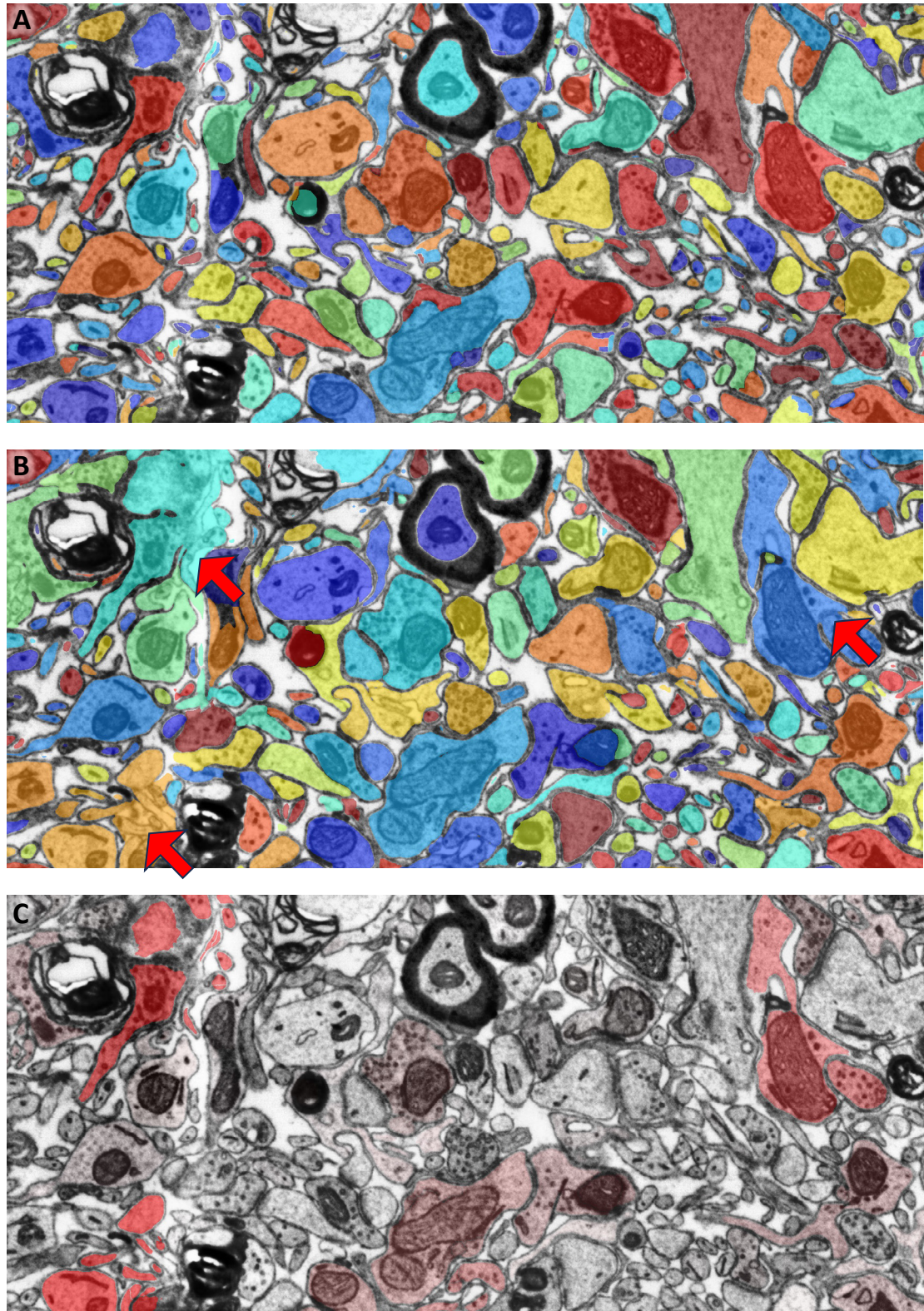


Figure S5. Ranking objects of two segmented images based on contribution to variation of information. **A.** Segmentation of long dwell time image at 1000 ns. **B.** Segmentation of short dwell time image at ~ 100 ns overlaid on 1000 ns EM. Some large errors are indicated with red arrows. **C.** Objects that vary between the two segmented images. Red heatmap indicates contribution to variation of information (Meila, 2003) where variable objects come from either of the two segmented images. The largest variation is captured by the three objects indicated by red arrows.

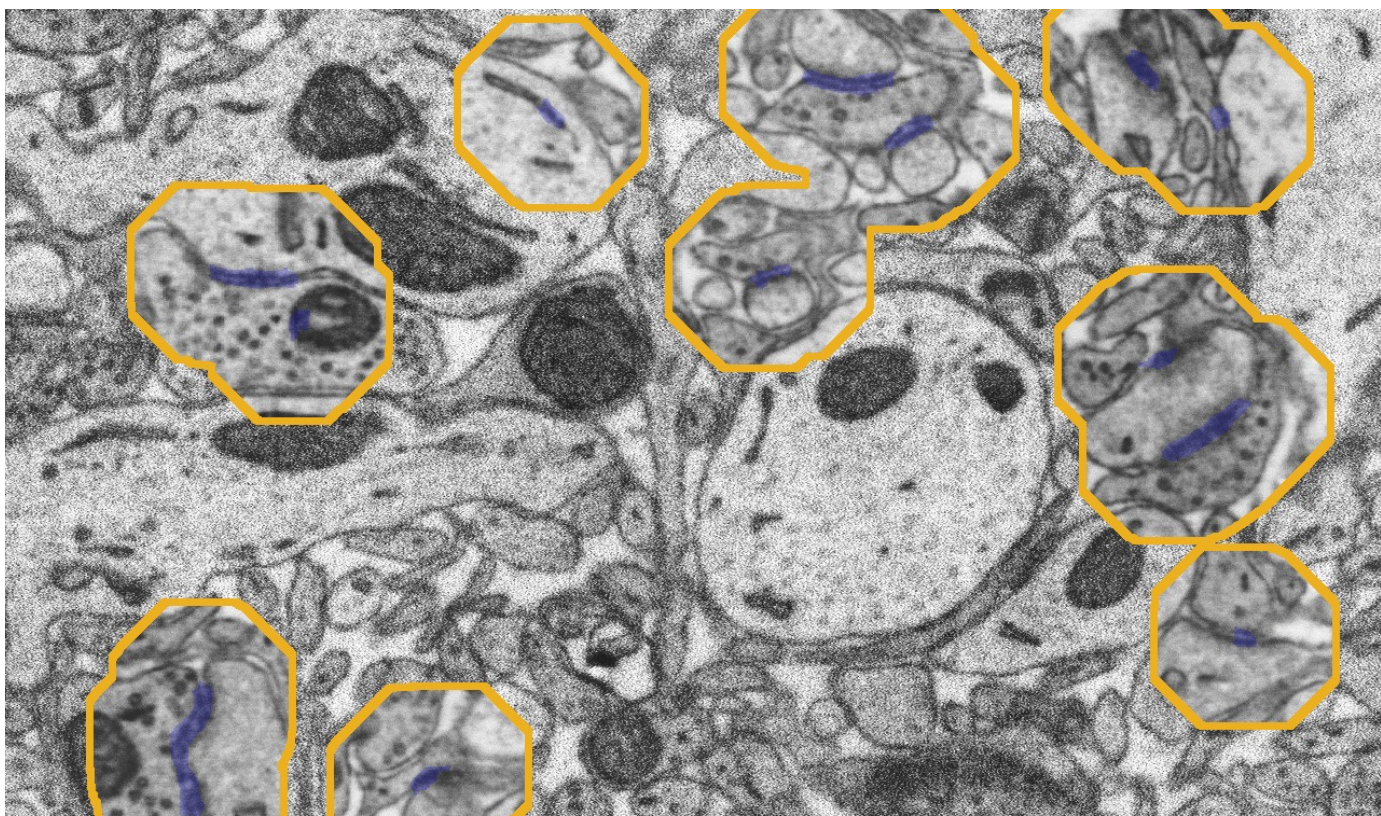


Figure S6. Data-aware imaging of synapses at long dwell time. SmartEM takes a short dwell time image (50 ns/pixel), predicts locations that contain synapses, and re-scans these regions at long dwell time (1200 ns/pixel). The blue overlay presents synapse predictions by MUSTINCLUDE. Yellow outlines represent locations for re-scan based on dilation of MUSTINCLUDE predictions.

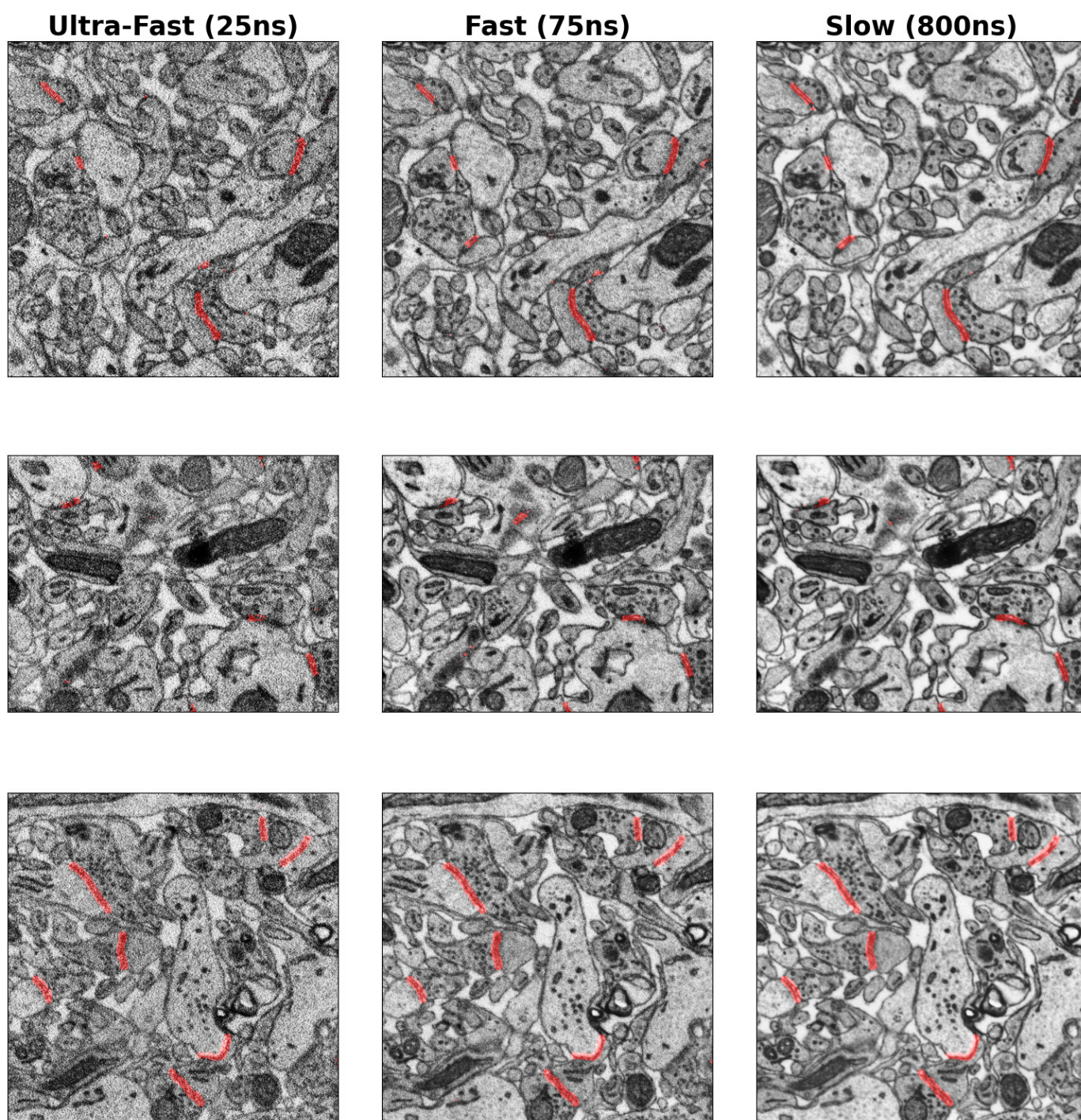


Figure S7. Synapse detection in ultrafast (25 ns), fast (75 ns) and slow (800 ns) dwell time. SYNAPSENET works at multiple dwell times.

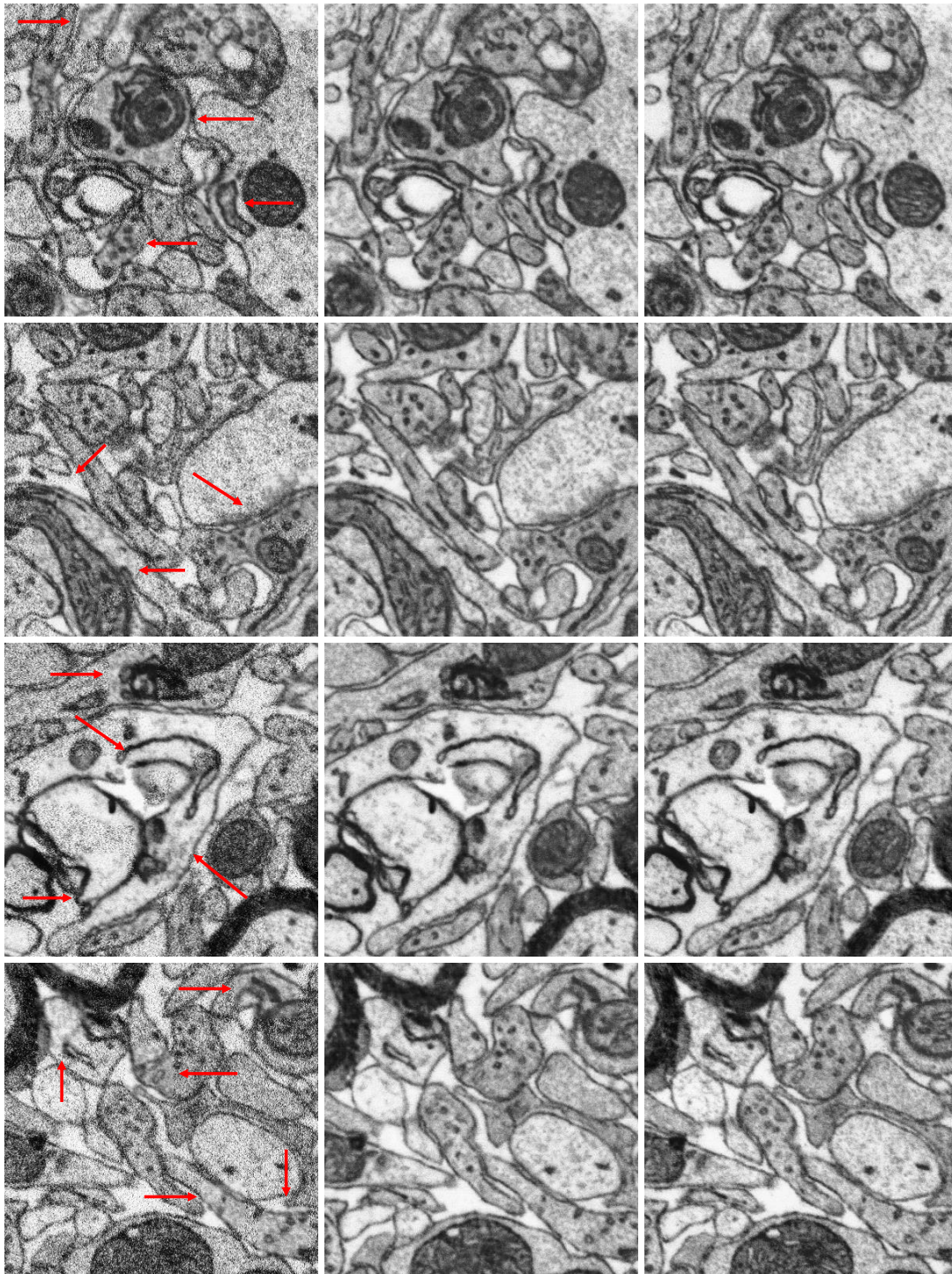


Figure S8. Examples of image homogenization by IMAGEHOMOGENIZER. Left column: composite EM with two dwell times (75 ns/pixel and 600 ns/pixel). Middle column: homogenized EM from composite EM, exhibiting similar visual coherence compared to slow EM. Right column: slow EM (600 ns/pixel). Red arrows indicate the locations with slow dwell time of 600 ns/pixel in composite EM.

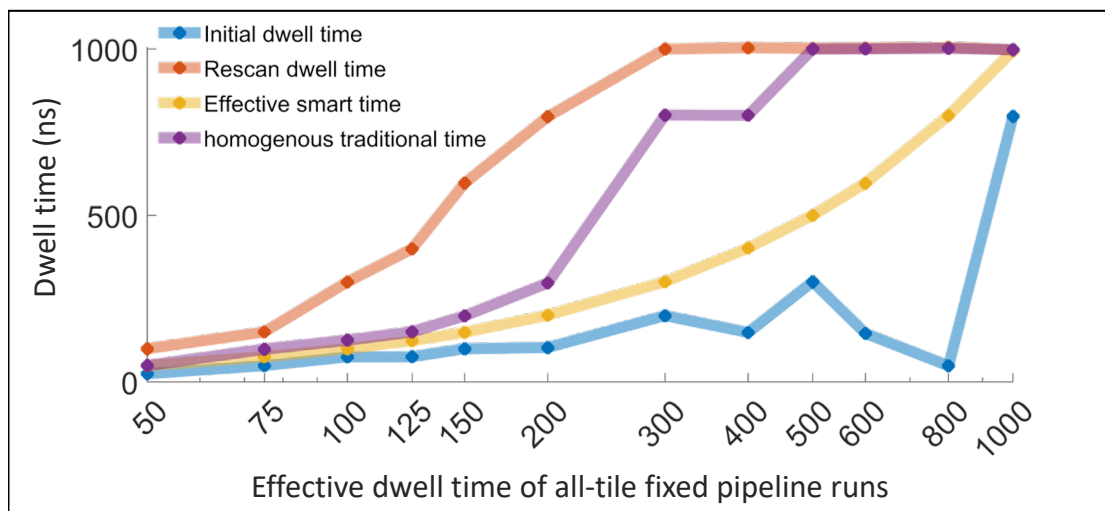


Figure S9. Globally fixed SmartEM parameters and their respective speedup compared to traditional EM.

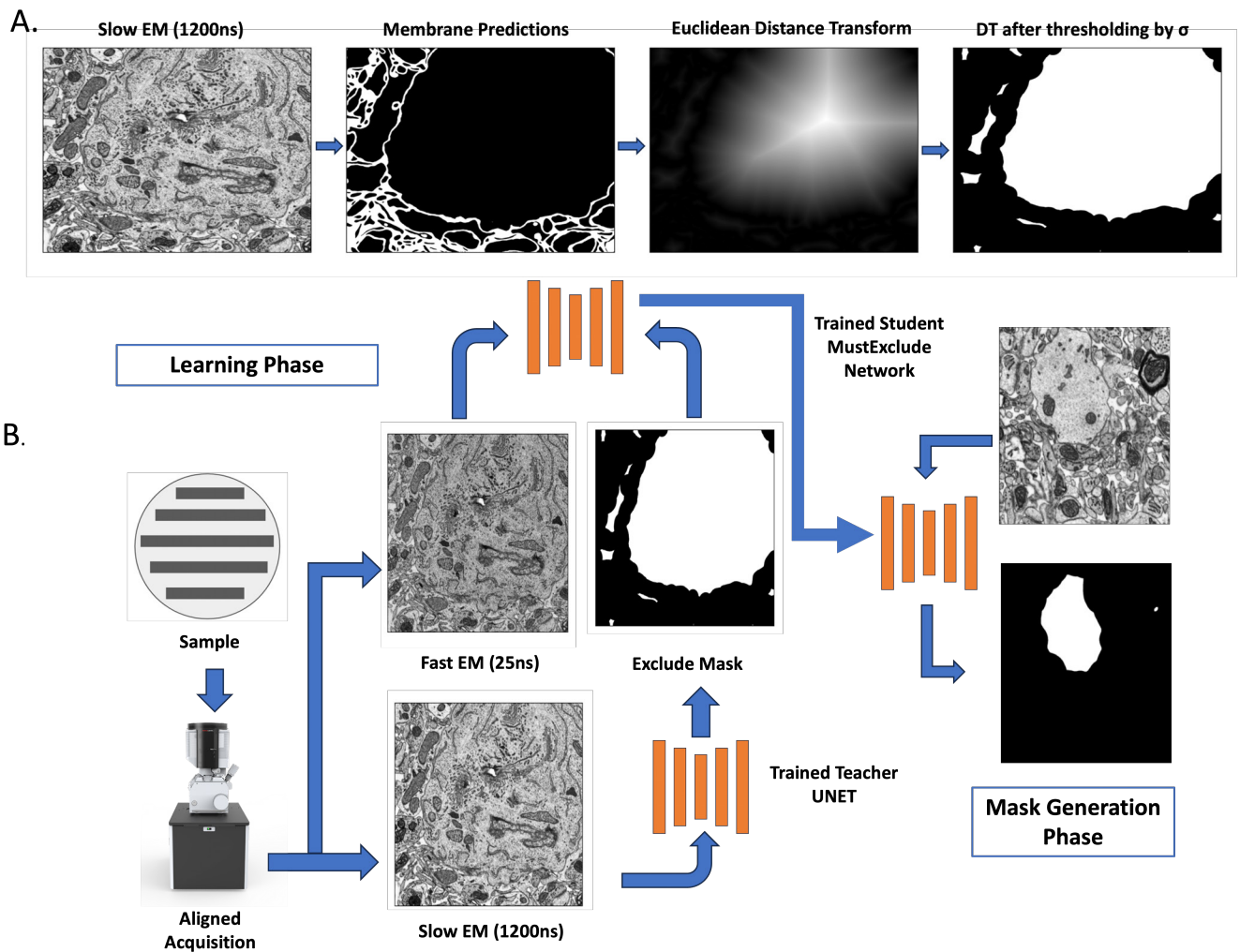


Figure S10. A. The process of generating the MUSTEXCLUDE ground truth. B. The paired Fast EM and the MUSTEXCLUDE mask generated are used to train the network which is deployed to generate the portions of EM to exclude in real time.

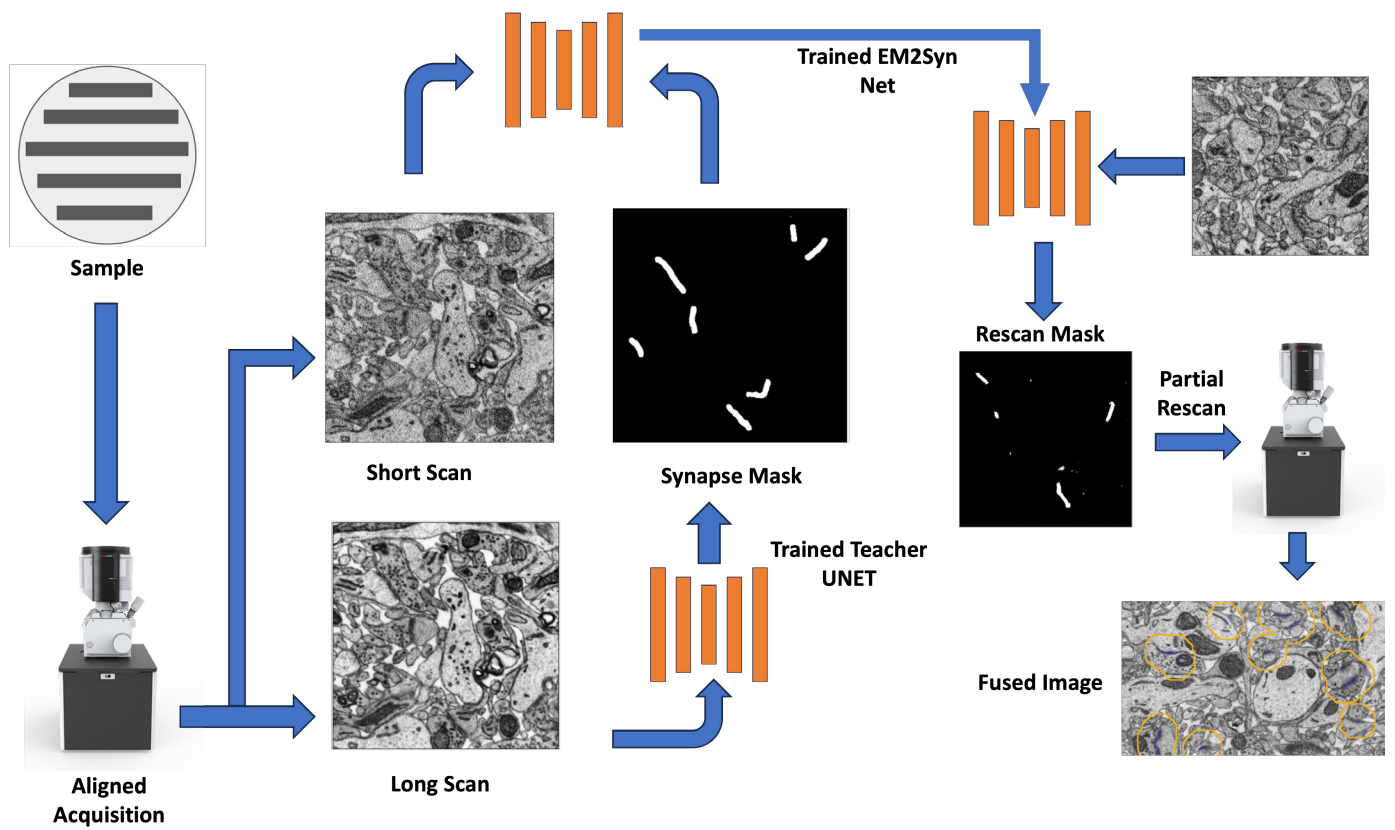


Figure S11. Synapse detection and rescan mask generation pipeline

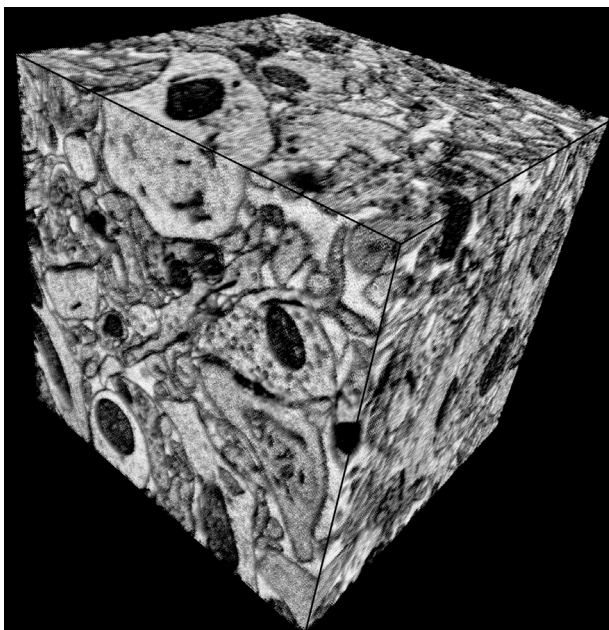


Figure S12. A cubical 3 μm portion of an aligned smart EM output from 94 serial sections.

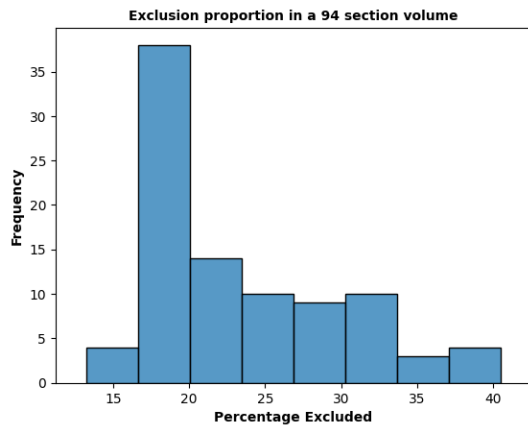


Figure S13. Percentage of EM that can be excluded in a $60 \times 68 \times 3 \mu\text{m}^3$ section. On average, around 23% of the volume can be excluded from rescanning.

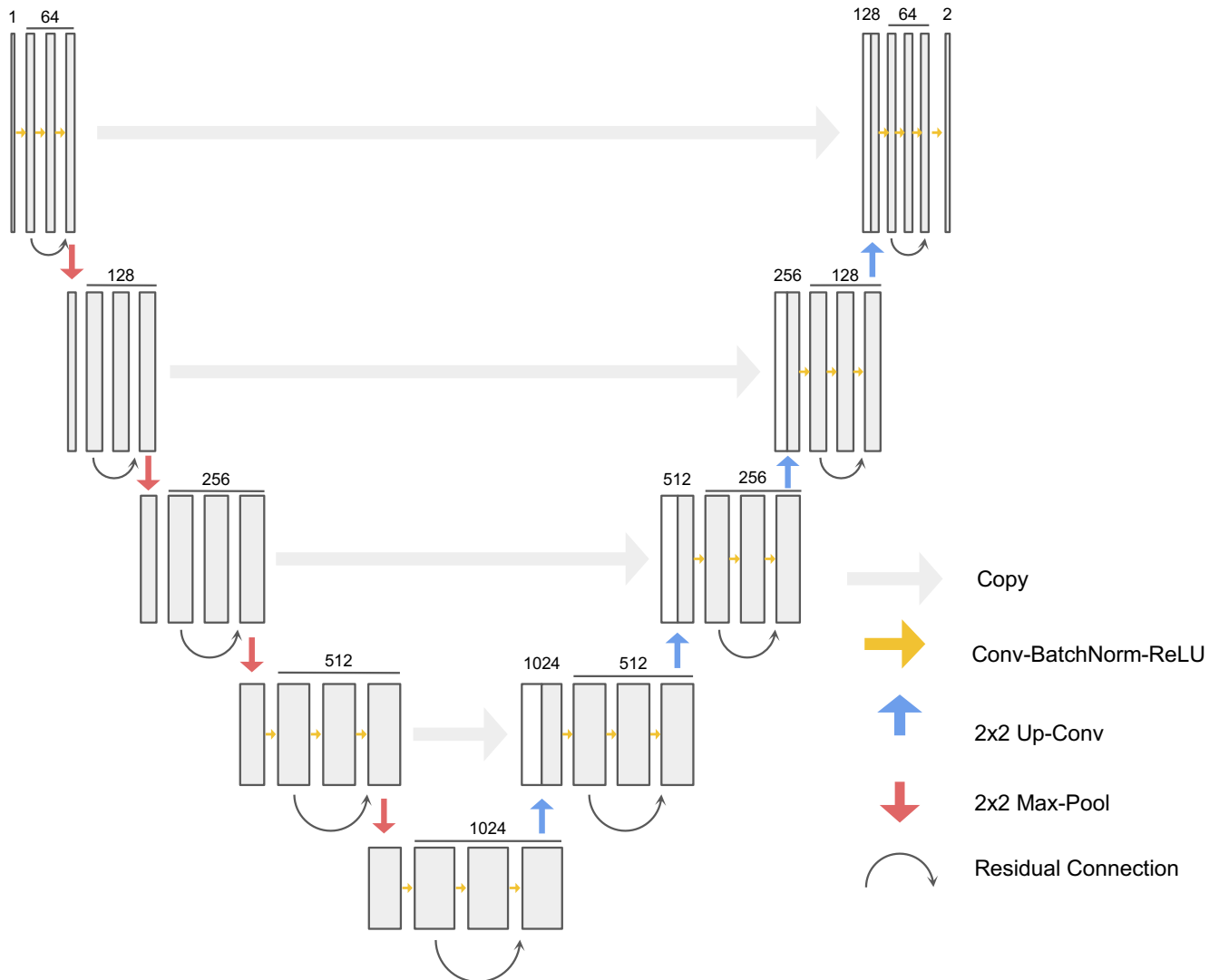


Figure S14. CNN architecture used for the FUSEDEM2MB and ERRNET. The architecture is similar to U-Net (Ronneberger et al., 2015), but has 3 layers of (Convolution, Batch-Normalization, ReLU) in each layer and has additional residual connections (He et al. (2016)). The architecture is fully convolutional and for both FUSEDEM2MB and ERRNET the input dimension is 1, respectively for the grayscale image and the membrane probability. In both cases the output dimension is 2, respectively for 0: not-membrane, 1: membrane and 0: no-error, 1: error